Determination of mineralization stages using correlation between geochemical fractal modeling and geological data in Arabshah sedimentary rock-hosted epithermal gold deposit, NW Iran

Peyman Afzal[a], Seyed Mehran Heidari[b,c,*], Majid Ghaderi[d], Amir Bijan Yasrebi[e,f]

[a] Department of Mining Engineering, South Tehran Branch, Islamic Azad University, Tehran, Iran
[b] Research Institute of Earth Sciences, Geological Survey of Iran, Tehran, Iran
[c] Geological Survey of Iran, National Geoscience Database of Iran, Tehran, Iran
[d] Department of Geology, Tarbiat Modares University, Tehran 14115-175, Iran
[e] Department of Mining and Metallurgical Engineering, Amirkabir University of Technology (Tehran Polytechnic), Tehran, Iran
[f] Computational Geomechanics Group, College of Engineering, Mathematics and Physical Sciences, University of Exeter, Streatham Campus, Exeter, UK

ARTICLE INFO

ABSTRACT

This research paper aims to delineate and recognize different gold mineralization stages based on surface lithogeochemical data using factor analysis and Spectrum-Area (S-A) modeling, as well as geological data in Arabshah sedimentary rock hosted epithermal gold deposit, NW Iran. Based on the factor analysis, Au and Mn were allocated to factor 2 (F2) and then classified by the S-A fractal modeling. In addition, Au and F2 values were transformed to spectrum data, which were categorized by the S-A log-log plots. Accordingly, the main mineralization phase contains Au and F2 (Au-Mn) values greater than 800 ppb and 0.3, respectively, and is associated with the occurrence of minerals such as pyrite, arsenian pyrite, realgar, orpiment and oxidized sulfides. The first phase of gold mineralization, where Au typically ranges between 80 and 350 ppb, is associated with base metal sulfides, arsenian pyrites and F2 values between 0.1 and 0.2. The second gold mineralization phase consists of Au values from 350 to 800 ppb and F2 values between 0.2 and 0.3. Combination of the S-A modeling, factor analysis and geological data outlined three gold mineralization stages in Arabshah gold deposit. The main mineralization stage showed a strong positive correlation with the NE-SW and NW-SE trending structures, the altered intrusive rocks such as microdiorite and granodiorite, and the altered subvolcanic dacitic domes.

1. Introduction

Mineral deposits are a collection of certain elements and minerals, therefore determination of the paragenetic minerals, geochemical suite elements and phase zoning in various stages of mineralization is very important to identify type of mineralization and carry out exploration activities. Delineation of different ore mineralization stages are particularly important for determination of enrichment zones. Mineralization phases and stages show a deposit's forming processes during the occurrence time which are recognized based on textural relationships and overprinting processes. Different methods have been used for mineralization phases and stages since the 1950s. The paragenetic sequence works with detailed microscopy studies in polished ore mineral section, petrologic thin section and SEM and EPMA studies as well as macroscopic field observations (Hedenquist et al., 2000; Groves et al., 2005; Goldfarb et al., 2007; Pirajno, 2009; Dill, 2011).

However, these methods are usually limited, therefore using quantitative data and mathematical equations with many variables can help in detecting the phase changes.

The sedimentary rock hosted epithermal Au/As/Sb (Pb-Zn) Arabshah deposit, is located about 27 km southeast of the town of Takab in northwest of Iran (Fig. 1). The Arabshah deposit is part of the hydrothermal gold mineralization system in Takab region which hosts Carlin-like, sedimentary rock-hosted gold deposits of Zarshuran and Aghdarreh and volcanic hosted epithermal gold deposit such as Touzlar. The main hydrothermal alteration and mineralization in Arabshah deposit are present in the form of sedimentary rock which hosts gold mineralization. This is associated with stratigraphic units of Zarshuran and Aghdarreh deposits (Mehrabi et al., 1999; Asadi et al., 2000; Daliran, 2008). According to different studies, the genesis of gold mineralization in this region is associated with Miocene felsic subvolcanic intrusion (Mehrabi et al., 1999; Asadi et al., 2000; Richards et al., 2006;
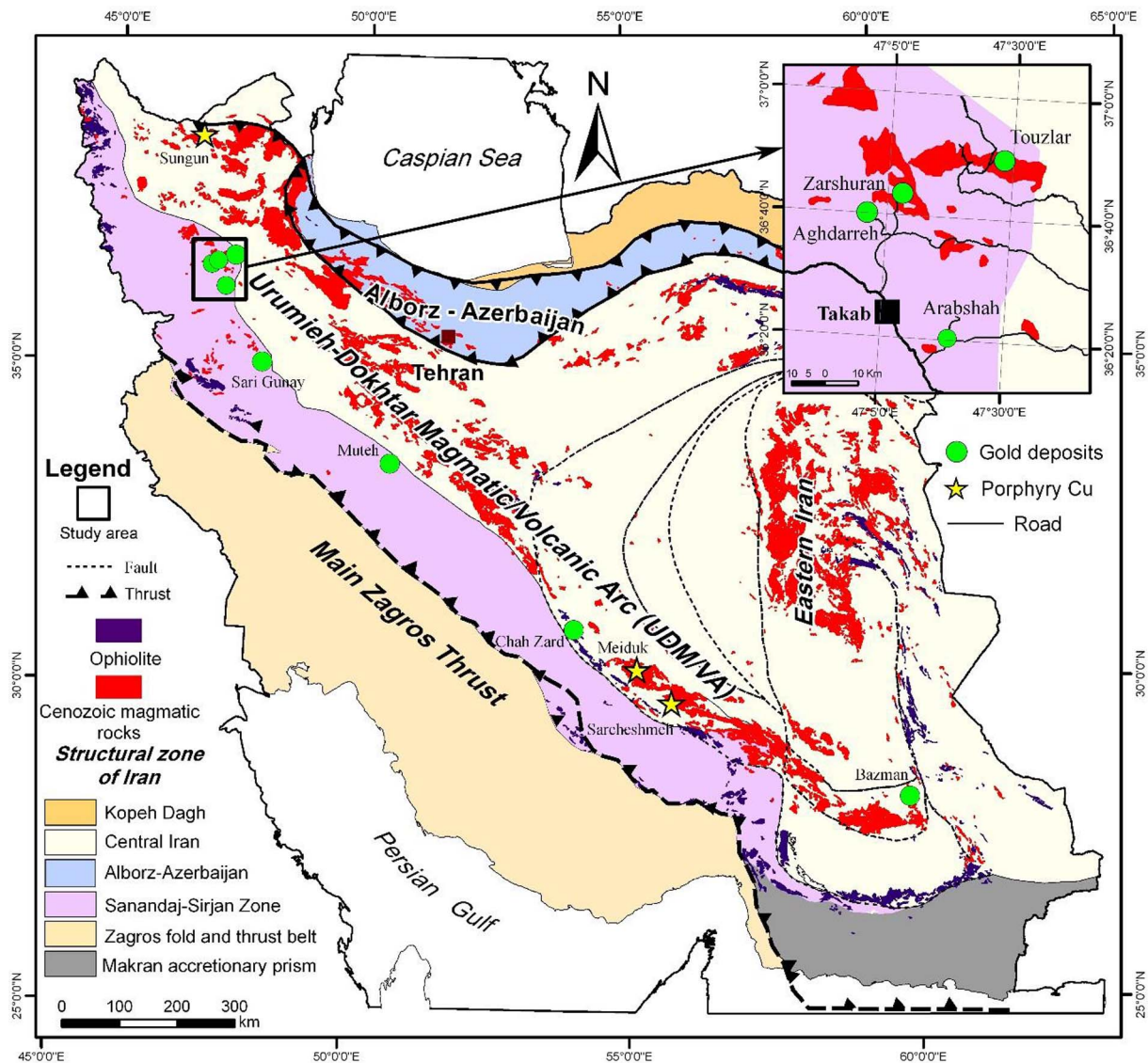
Fig. 1. Location of the Arabshah and some of important epithermal gold and porphyry copper deposits in the Urumieh–Dokhtar arc, which runs parallel to the main thrust of Zagros with the Sanandaj–Sirjan metamorphic-magmatic zone and ophiolite belt compiled based on the 1:2,500,000 digital geologic map of Iran (GSI, 2006; Berberian and King, 1981; Bonini et al., 2003; Mohajjel et al., 2003; Richards et al., 2006; Shafiei et al., 2009; Heidari et al., 2015).

Heidari et al., 2015).

Several ancient mining activities exist in the area and surficial orpiment/realgar minerals were mined in the 1960s. However, exploration activities for gold including geochemical survey, geological mapping of 1:5000 and 1:1000, trenching and drilling were carried out between 1995 and 2005. Based on systematic geochemical sampling (soil and rock) in the study area, gold mineralization is related to quartz veins and their altered wall rocks (Karamsoltani et al., 2004). Gold particles are invisible in this deposit and in other sedimentary rock hosted deposits located in this region (Daliran, 2008; Asadi et al., 1999).

Fractal/multifractal modelling established by Mandelbrot (1983) which has been widely utilized for separation of different geological, geochemical and geophysical populations (e.g., ore grade; Turcotte, 1986; Bolviken et al., 1992; Cheng et al., 1994, 1999; Agterberg, 1995; Sim et al., 1999; Li et al., 2003; Zuo et al., 2009, 2013; Zuo, 2014; Afzal et al., 2011, 2012). Importantly, these studies show that the distribution of ore elements has a fractal behavior. In other words, recent investigations of geochemical features have shown that self-similarity or self-affinity are significant properties of geochemical data on different scales from microscopic to continental.

The fractal/multifractal models have been proposed and applied to geochemical data for the separation of anomalies or mineralized zones from background as well as determination of different mineralization stages (Cheng, 2000; Carranza, 2009; Carranza and Sadeghi, 2012; Gumiel et al., 2010; Afzal et al., 2013a; Heidari et al., 2013; Carranza et al., 2015; Nazarpour et al., 2015; Zuo and Wang, 2016; Zuo et al., 2015; Parsa et al., 2016a, b). The common fractal models are concentration-area (C–A) and perimeter–area (P-A) models (Cheng et al., 1994), concentration-distance (C–D) model (Li et al., 2003), number-size (N–S) model (Mandelbrot, 1983; Agterberg, 1995), power spectrum-area (S-A) model (Cheng et al., 1999), concentration-volume (C-V) model (Afzal et al., 2011) and simulated size–number (SS–N) model (Sadeghi et al., 2015). The concept of multifractal singularity mapping in geochemical analysis has been particularly studied (Cheng, 2007; Cheng and Agterberg, 2009; Zuo and Cheng, 2008; Zuo et al., 2012). Heidari et al. (2013) used the C-A multifractal modeling for separation of mineralized phases based on lithogeochemical data in Touzlar epithermal Au-Ag (Cu) deposit, NW Iran.

Multivariate statistical models including factor and clustering analyses are appropriate approaches to classify and reduce the number of geochemical variables (Muller et al., 2008; Yousefi et al., 2012, 2014;
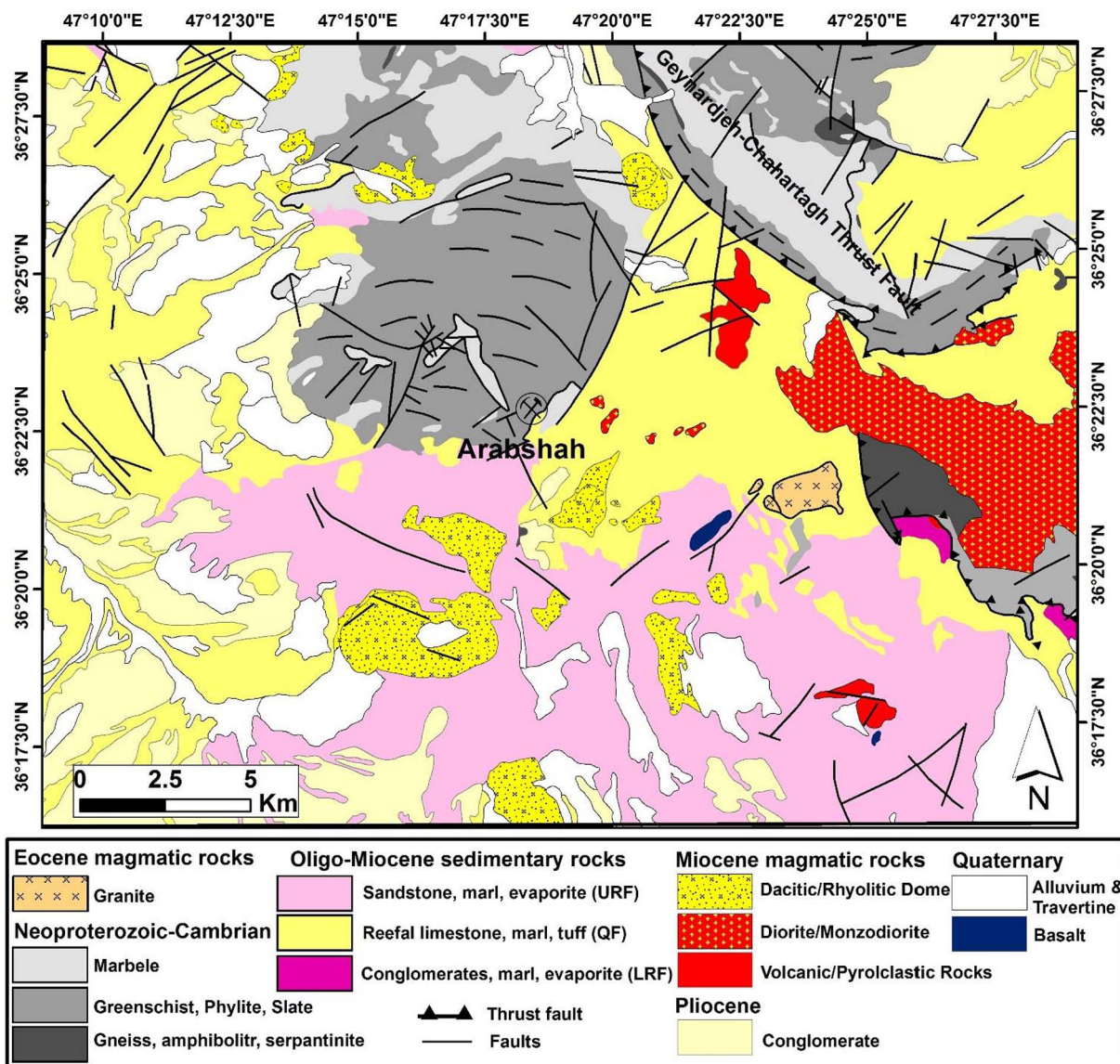
Fig. 2. Geological map of Arabshah region with location of Arabshah deposit within the basement metasedimentary rocks, based on 1:100,000 geological maps of Takab (Fonoudi et al., 1998).
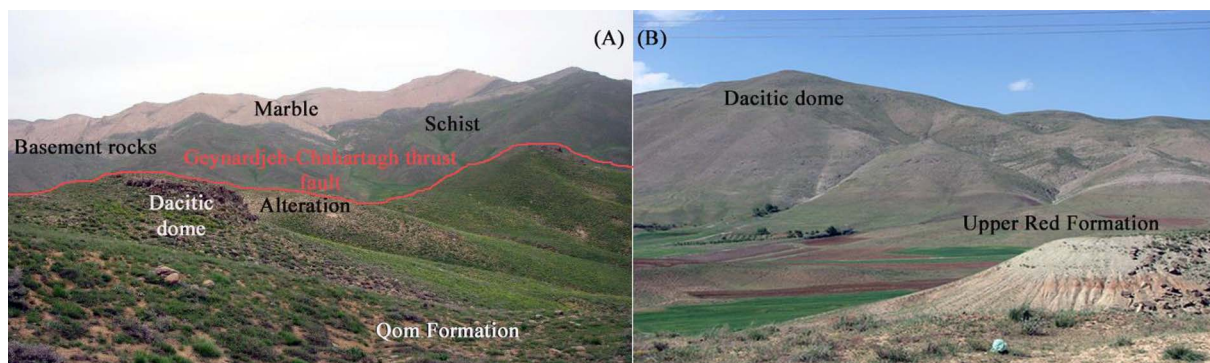

Fig. 3. Field photographs of the sedimentary basement and Qom Formation in Arabshah area. A) Marble and schist units of basement rock thrusted on the Qom formation and dacitic dome in the west of Geynarhjeh fault in Fig. 2, looking from northeast. B) Dacitic dome penetration of Upper Red Formation, with looking from the north (the deposits is located behind the dome).

Zuo et al., 2009; Zuo 2011, 2014; Yousefi, 2016; Yousefi and Carranza, 2015). Factor analysis is one of the regular multivariate analyses which demonstrates a powerful implement to visualize high dimensional data in lower dimensional spaces based on variance and covariance matrix.

In this paper, a hybrid method via the S-A fractal model, factor analysis and geological modeling was conducted for the separation of stages of Au mineralization, based on lithogeochemical, mineralogical and alteration data in Arabshah deposit, NW Iran. This paper is

Fig. 4. Field observation from hydrothermal alteration zone in Arabshah and jasperoids. A) The SW-NE trending zones of Arabshah hydrothermal alteration and mineralization in metasedimentary rocks; B) Close view of some the parallel quartz veins with their peripheral alteration; C) Silicic alteration vein which are controlled by the NE-SW trending fault; D) The lattice structures of jasperoids surrounding carbonate rocks and E) Remnants of the first phase of silicic alteration.

organized in four parts after "Introduction". Methodology follows a brief discussion of the S-A fractal model and factor analysis. The case study explains "Geological setting" including regional and local geology especially mineralization and alteration features. Subsequently, assay quality control and geochemical dataset are described and statistical and geostatistical interpretation are carried out based on lithogeochemical data. Moreover, the combination of geological data, the S-A fractal model and factor analysis was applied to lithogeochemical data for determination of gold mineralization stages. "FPSA" software is implemented in MATLAB coding environment (Afzal et al., 2013b) to apply the S-A fractal model for results obtained via factor analysis. Ultimately, the Au mineralized stages are correlated with significant geological data consisting of mineralographical data, silicic veins and hydrothermal alteration zones.

2. Methodology

2.1. Power spectrum-area fractal method

Fourier and inverse Fourier transformations (FFT and IFFT) have been usually utilized in time series analysis and signal processing (Cheng et al., 1999; Cheng, 2007; Zuo, 2011; Afzal et al., 2013b; Parsa et al., 2016b). Spectral energy density functions demonstrate the power

spectrum distribution in the frequency domain. The advantage of dealing with fields in the frequency domain is that some complex convolution operations in the spatial domain for correlation analysis, filtering, and transformation can be simplified significantly in the frequency domain (Cheng, 2007).

Cheng et al. (1999) proposed spectrum-area (S-A) model to denote the power-law frequency distribution of the power spectrum density which is suitable to separate geochemical anomalies from background. A new function relating the multifractal model and the spectral-energy-density function were derived to indicate the power-law relationship between the spectral-energy-density value (S) and the "area" of the set $\Omega(\geqslant S)$ with spectral-energy-density values above S on the power-density plane. The model has the general form as following formula (Cheng, 2004, 2006):

$$A[\Omega(\geqslant S)] \propto S^{-2d/s} \tag{1}$$

where 2d is related to the so-called elliptical dimension with d = 1, corresponding to isotropic dimension and s > 0, the exponent of the power law. With the S-A model the power spectrum density field can be distinguished into components with distinct self-similarities that can be converted back to the space domain to correspond to decomposed patterns with distinct generalized self-similarities. The power spectrum multifractal modeling have been studied based on stream sediments,
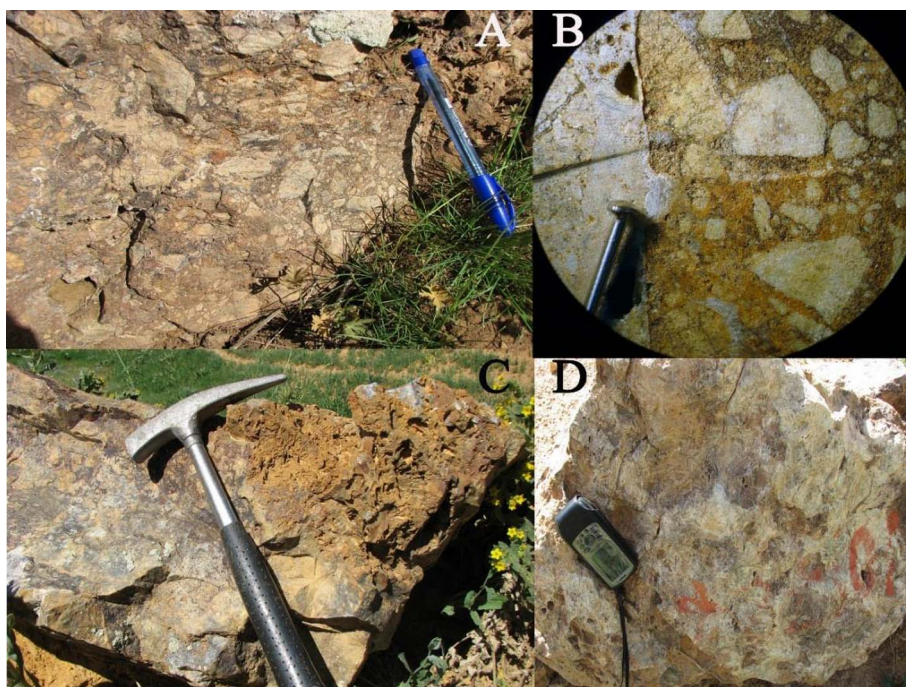
Fig. 5. Photographs from second phase of hydrothermal silicic alteration. A) Hydrothermal breccias consisting of quartz angular fragments of carbonate host rocks in quarts matrix; B) Close view of the hydrothermal breccias with angular fragments of the first phase of silicification; C) Space filling of second phase of silicification with white color within porous jasperoids vein and D) Massive quartz vein generated via filling phase 2 in lattice structures of first silicification phase.
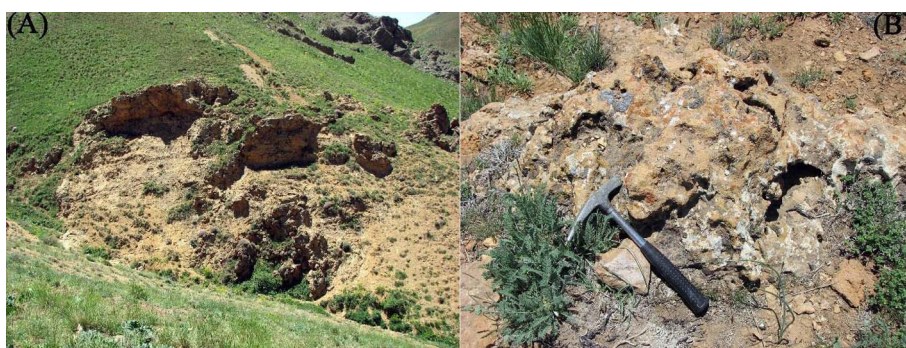

Fig. 6. Decalcification and sanding alteration: A) In the southern part of the study area and B) In outcrop with voids in surface.

lithogeochemical and drillcores (e.g., Ali et al., 2007; Afzal et al., 2012, 2013a; Zuo, 2011, 2012; Zuo et al., 2015; Zuo and Wang, 2016).

2.2. Factor analysis

The factor analysis is an applicable approach for combining several correlated variables into a single variable for reducing the dimensionality of datasets into uncorrelated principal components based on covariance or correlation of variables which represent the inter-relationships within the multi-dimensional data (Jolliffe, 2002; Reimann et al., 2005; Zuo, 2011; Shamseddin Meigoony et al., 2014; Wang and Jiao, 2014; Yang and Cheng, 2015). Based on this technique, a large dataset of geochemical variables is combined in a few factors. In this method, the dataset (elemental concentration in this scenario) is divided into several subsets which are indicated by various factors. Factors are demonstrative for geological and ore-forming processes (Krumbein and Graybill, 1965; Johnson and Wichern, 2002; Muller et al., 2008; Zuo, 2011; Wang and Jiao, 2014; Wang et al., 2010, 2015).

2.3. Conceptual model of sedimentary rock hosted epithermal gold deposit type

These gold deposits have multi-stage mineralization paragenesis with at least one stage which consists of stockwork-disseminated or sheeted vein zones (Berger, 1986; Goldfarb et al., 2005; Robert et al., 2007). Hydrothermal alteration include sericitization, carbonatization, silicification, sulfidic and biotitic alteration which may extend for considerable distances around ore deposits. Muruntau is the largest deposit of this class which contains 200 Moz of gold. Moreover, the main stage of gold mineralization in this deposit consists of sheeted quartz-feldspar veins with As, W, Sb, Bi, and Mo (Wall et al., 2004). In addition, these gold deposits have important structural controls and are commonly located in the core of anticlines intersected by high-angle faults (Robert et al., 2007).

3. Geological setting

3.1. Regional geology

The sedimentary rock hosted epithermal Au/As/Sb (Pb-Zn) Arabshah deposit, as well as other important gold deposits in the NW Iran, is related to Cenozoic Urumieh-Dokhtar magmatic arc (UDMA; Fig. 1). Formation of this magmatic belt is related to the closure of Neothetys between Arabian and Eurasia plates from Triassic-Jurassic to Neogene (Glennie, 2000; Alavi, 1994, 2004; Allen, 2006; Ghasemi and Talbot, 2006; Agard et al., 2011).

Hydrothermal activity related to the UDMA is present within some parts of Sanandaj-Sirjan Zone and Central Iran which hosts various mineralization types such as porphyry copper (Sar-Cheshmeh, Meiduk, Sungun) and epithermal gold deposits (Sari-Gunay, Muteh, Touzlar,
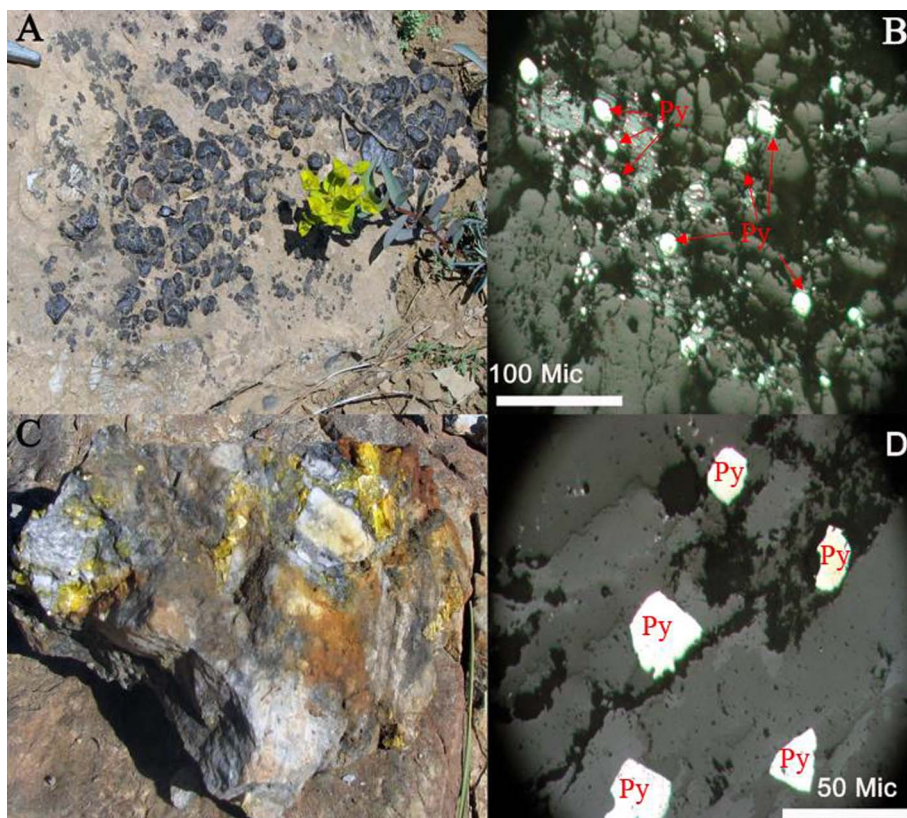
Fig. 7. Sulfidic alteration: A) Coarse grain of pyrite in the surface of carbonate rock; B) Aggregates of pyrites (Py) in quartz which have become to Fe-oxide in margin; C) Realgar in hand specimen and D) Sulfides mainly pyrite (Py) and arsenian pyrite in fractured quartz.

Chah-Zard, Bazman; Fig. 1).

Uplifting and exposure of basement rocks play an important role in the geodynamic evolution of this region. Based on studies by Stockli et al. (2004), an extension phase was followed by rapid exhumation of Neoproterozoic–Cambrian metasedimentary rocks as metamorphic core complexes within low-angle detachment faults. Based on geo- and thermochronological studies, mineralization processes occurred during Oligo-Miocene (Stockli et al., 2004; Verdel et al., 2011).

3.2. Local geology

Ore hosting Neoproterozoic–Cambrian metasedimentary rocks in Arabshah are located in the eastern and northern parts of the study area with dips of between 20° and 50° towards the south (Fig. 2). The basement units consisting of low-grade metamorphic rocks, mainly schist with intercalations of bedded dolomite (passing up through grey to cream dolomite with schist intercalations) are overlain by cream to light brown massive dolomite (Gilg et al., 2005). In addition, some units have been thrusted westwards onto the Neogene units (Figs. 2 and 3A). Paleozoic and Mesozoic sedimentary rocks in this area are limited to the west of the uplifted basement (Fig. 2). Sedimentation in this area commenced from Oligo-Miocene with sequences of clastic deposits and Lower Red formation (LRF) in the form of basal conglomerate, sandstone and marl (Ghalamghash and Babakhani, 1992) which are located over basement uplifted units, with outcrops in the marginal parts of basement rocks and faults (Fig. 3).

The LRF is followed by the Qom formation (QF) which is composed fine-grained clastic sedimentary rocks with marl, tuff and reef limestone of lower Miocene ages (Fig. 3A). The QF is covered by a series of rocks including evaporite-bearing red marls, sandstones and conglomerates (Fig. 3C, Fonoudi et al., 1998) which belong to Upper Red Formation (URF). Moreover, the east part of the area was intruded by upper Miocene shallow intrusives such as microdiorite, granodiorite and dacitic domes (Figs. 2 and 3B). The upper Miocene sediments of the URF have been covered by Paleocene and Quaternary polymictic conglomerate, travertine, fluvial and alluvium deposits. Rare igneous activity with basanite composition is present in this area (Daliran et al., 2009).

Based on systematic drilling, the proved ore reserve at Arabshah is 1.5 Mt of oxide ore with 1.2 g/t Au. The gold mineralization is mostly associated with the jasperoid veins with 600 m length and 0.5–2 m width (Karamsoltani et al., 2004). The prominent structural features in Arabshah area follow a NW-SE trend. This trend follows the major Geynardjeh-Chahartagh thrust fault, as shown in Fig. 2.

3.3. Alteration

Hydrothermal alteration in the NE trending at Arabshah is associated with dacitic domes and it covers an area of 1–2 km^2 mainly within calcschist, dolomite and marble (Fig. 4A, Heidari, 2013). Field mapping, microscopy study and XRD analysis were performed leading to the recognition of five hydrothermal alteration assemblages consisting of silicification, decalcification, sulphidization, dolomitization and minor argillic alteration. The inner alteration zone is characterized by silicification and sulphidization, which are associated with gold deposition (Fig. 4A). The most important type of hydrothermal alteration in this area, which leads to the formation of large amounts of jasperoid, is silicic alteration. This is present in the core of the hydrothermal alteration system (Fig. 4A). Silicification also consists of subparallel, steeply dipping quartz veins (Fig. 4B). These veins were controlled by extensional fault and fracture systems, trending in EW to NE-SW directions (Fig. 4C). The hydrothermal fluid flow was channeled within these structures thereby controlling the mineral and alteration system of the area. Gold mineralization is often associated with silicification although there are some barren jasperoids. Weak to strong silicification varies with respect to the permeability of host rocks and hydrothermal fluids. In addition, there is a linkage between various size and textures of quartz grains and the distance from the hydrothermal channels.

Silicic alteration in the Arabshah deposit is of two types:

| Minerals	Hydrothermal Alteration				Post Mineralization (Oxide Stage)
	Pre Mineralization	Mineralization			
	Stage 1	Stage 2			Stage 3
		Ph. A	Ph. B	Ph.C	Ph. D
Ore					
Pyrite	----	▬	▬	▬	
Arsenian pyrite	----	―	▬	▬	
Gold	----	―	▬	―	
Electrum		▬	----		
Chalcopyrite		▬	··········		
Chalcocite					―
Covellite					―
Galena		▬			
Sphalerite		▬			
Fe-Mn Oxide	―				▬
Malachite					▬
Azurite					▬
Realgar				▬	
Orpiment				▬	
Stibnite			▬		
Sulfosalts			―		
Smithsonite					▬
Cerussite					▬
Rhodochrosite					▬
Siderite					▬
Ankerite					▬
Gangue					
Quartz		▬	▬	―	
Sericite		―	―	―	
Carbonate		▬	―		
Gypsum					―
Jarosite					―
Kaolinite		―			―
Chlorite					―
Epidote		―			―
Illite		―	―		―
Montmorillonite		―	―		
Barite		----	----	▬	―
Alteration					
Silisification		▬	▬	▬	
Decalcification		▬			
Sulphidization	―	▬	▬	▬	
Dolomitization	▬	▬			
Argillic	―	▬			

Fig. 8. Paragenetic scheme with relative abundances of alteration and ore minerals in different zones at Arabshah deposit.

replacement and open space filling. Replacement type formed the first with the main jasperoid veins with a thickness of about 1-2 m black to dark red in color (Fig. 4B, C). Based on the intensity of fractures in the host rock, the replacement process resulted in various structures and textures including veins and stockwork (Fig. 4D and E). The lattice structures are mainly hosted by fragments of carbonate rocks (Fig. 4D). The early jasperoids contain low sulfides, mainly pyrite. This type of silicification occurs earlier than decalcification, while dolomitization is simultaneous with silicification.

The second phase of silicic alteration was influenced by hydrothermal fluids as veins which was generated by the open space filling and hydrothermal breccias, crustiform, comb, cockade and mosaic textures (Fig. 5A, B). This silicification phase was followed with the first phase. In most cases, filling spaces have been created by the previous alteration phases including decalcification, dolomitization and argillic. However, this was not seen in all segments for the first phase of mineralization (Fig. 5C).

Quartz in this stage are fine grained and light-colored which were filled by voids and cavities of host altered carbonate rocks (Fig. 5D). In this stage, hydrothermal breccias were dominated and they typically contain quartz-matrix within angular centimeter-scale fragments of carbonate host rocks (Fig. 5A, B). Most of the breccia fragments are monomictic with size between 0.1 and 5 cm with jigsaw-fit textures. This matrix is commonly composed of quartz with minor fraction of very fine grained (0.01 mm) which are well-cemented (Fig. 5B). The sulfides are mainly fine grained, disseminated and rarely massive
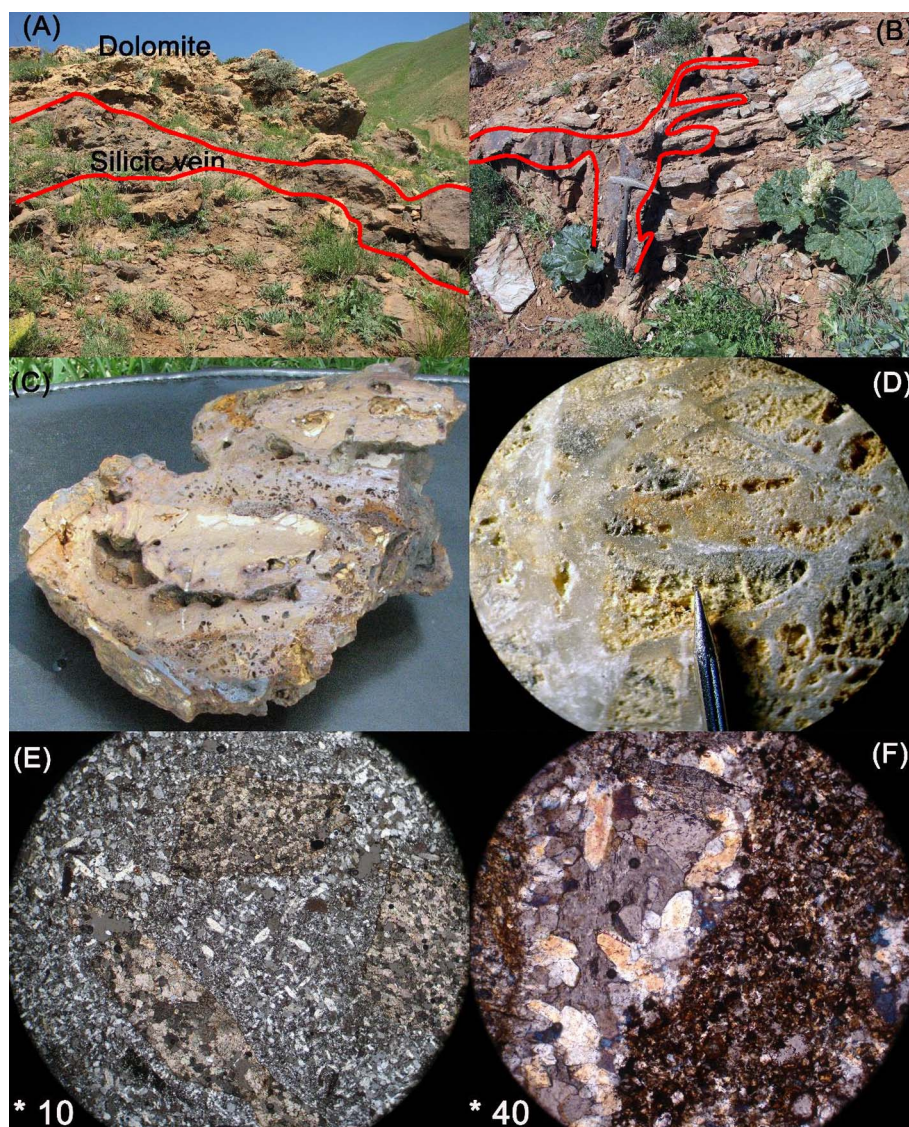
Fig. 9. View of silicification of the phase A (jasperoid) which is associated with dolomitization and sulfide mineralization in outcrops: A) Quartz veins and dolomitization in the surrounding areas of quartz veins within the host rock B) Quartz vein of phase A which is cut the foliation and schistosity of the carbonate rocks, C and D) Jasperoids and dolomitization observed in field and binacolar E and F) Accumulation of sulfide mineralization as fine grain disseminated sulfide within quartz and as massive sulfide in the dolomite in microscopic image.

within the host rocks. The characteristics of this alteration is similar to the argillic alteration. The silicification phase contains arsenic, antimony and minor zinc sulfides, pyrite and arsenian pyrite.

Decalcification is the most abundant alteration, especially in the southern part of the study area. This alteration is associated with siliceous zones in contact with the dacitic dome (Fig. 6A). The alteration was peripherally developed within the main NE-SW trending faults. Decalcification was resulted from removal of calcite predominantly from marble and calcschist by reaction of acidic hydrothermal solutions. The dissolution of calcite from host rocks led to the formation of cavities, porous and micro karsts (Fig. 6B). This process plays an important role for increasing of permeability for the host rocks of precious metals deposits. In addition, this process is affected by hypogene hydrothermal fluids within the sedimentary host rocks (Berger and Bagby, 1991; Mehrabi et al., 1999). Releasing of Fe-Mn oxides in the altered carbonate rocks is another characteristic of this alteration which is important in sulphidization formation.

Presence of disseminated sulfides, mainly pyrite in jasperoids, shows that sulphidization is related to hydrothermal alteration (Fig. 7). Sulphidization is usually accompanied by silicification in dacitic domes. Principal sulfide minerals commonly contain pyrite, arsenian pyrite, realgar, orpiment, galena, sphalerite and rare chalcopyrite which varies between very fine grained to invisible forms (Fig. 7). Most sulfides were oxidized to iron oxides by supergene process. The most intensity of

supergene processes occurred in the proximity of fractures and highly altered host rocks.

Another type of hydrothermal alteration is dolomitization. This type usually occurs in the early stages of alteration, limited to jasperoid replacement. Dolomitization is characterized by dark color which is resulted from precipitation of iron and manganese oxides after the silicic alteration within carbonate host rock. Pyrite is the common sulfide mineral which is associated with dolomitization.

Intermediate argillic alteration in the Arabshah is rare and mainly limited to dacitic domes. However, this type of alteration with lesser intensity occurs close to siliceous veins within carbonate host rocks (Fig. 8). Argillic alteration consists of various fine grained clay minerals such as kaolinite, illite and montmorillonite as detected by XRD analysis.

Supergene weathering in the Arabshah, especially in the fractured zones, caused acid leaching within limestone and precipitation of complex hydroxide minerals. Hydroxide minerals in supergene zone filled cavities in jasperoids and were replaced within limestone. Abundant Fe-oxides and hydroxides, clay minerals, gypsum, scorodite, azurite and malachite were formed during the supergene stage. The alteration sequence in the Arabshah epithermal system reflect the progressive neutralization of the fluids by the wall rocks same as highly acidic fluids.
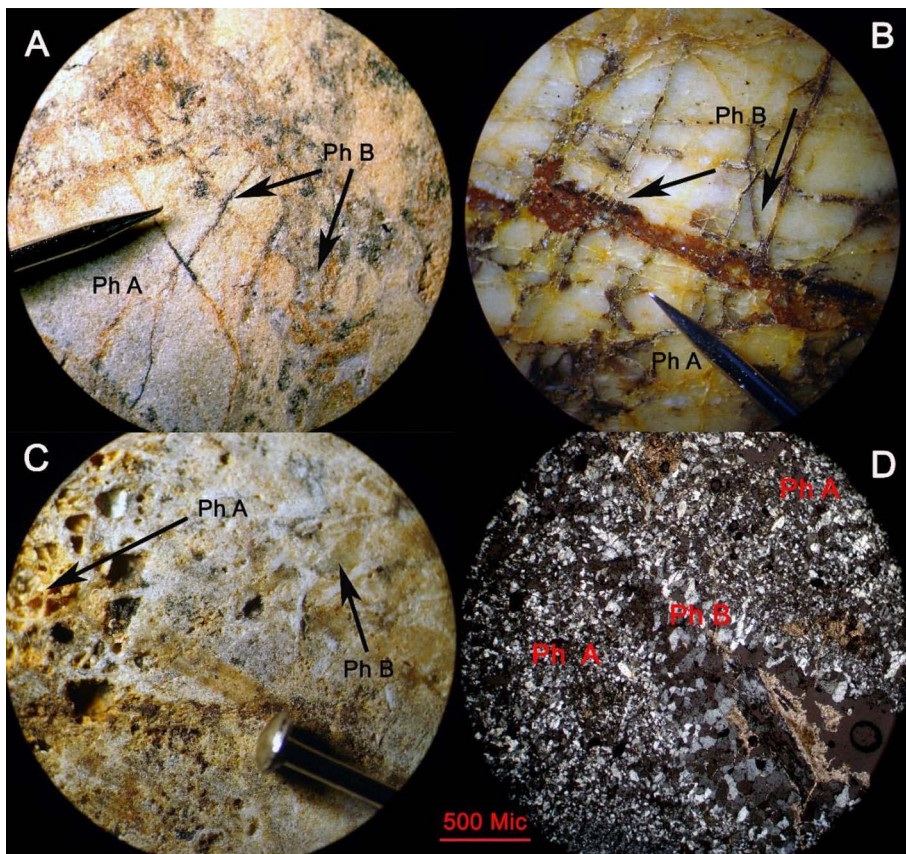
Fig. 10. The effect of Phase B in the second stage of the hydrothermal system of Arabshah.
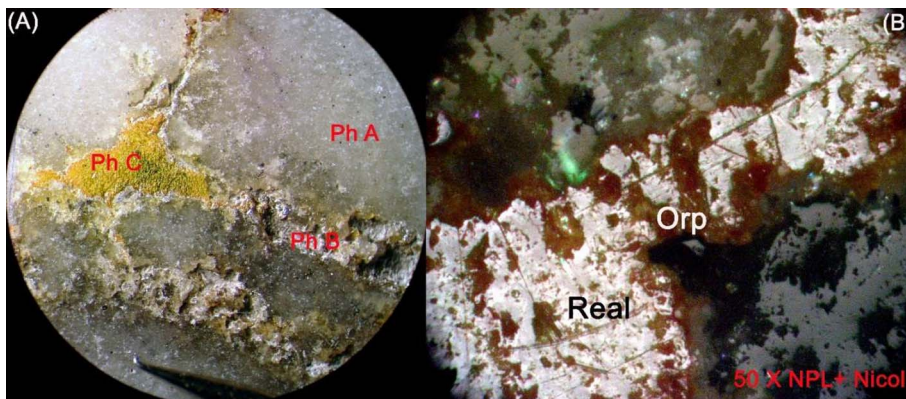

Fig. 11. Mineralization associated with the hydrothermal system phase C of the second stage: A) View of phases A, B, C in a section, A phase composed background, B phase located in fractures of A phase, C phase filled fractures that are not occupied by B phase B) Microscopic view from filling voids by realgar phase C.

3.4. Mineralization

According to the analyzed samples from the trenches, boreholes and soils, the main host rocks for epithermal gold mineralization in the Arabshah deposit are related to pervasive hypogene silicification and narrow halos of the wall rock alteration (Karamsoltani et al., 2004). These results suggested high correlation between gold grades and steeply dipping jasperoids and silicified hydrothermal breccia zones up to 5 m width and 400 m length (Heidari, 2013). The existing ore in the study area is not restricted to lithological units such as calcschists, marbles and a little amount of schists. Gold grade mean was measured about 0.34 ppm, with a maximum of 5.9 ppm (Heidari, 2013). Gold in the Arabshah and other similar deposits in this region is invisible and found as solid solution in the sulfide phase (Mehrabi et al., 1999; Asadi et al., 2000; Daliran, 2008; Heidari, 2013).

Sulfides, oxides, carbonates and sulfates of metals such as Fe, Mn, Zn, Pb, Cu and Ba with gangue minerals such as sericite, gypsum, chlorite, epidote, clay minerals and gold were identified within the mineralization zone. Their formation can be classified as following stages (Fig. 8):

Stage 1 (pre-mineralization stage): Extensive porosity and permeability of the host rocks were resulted from the reaction of acidic hydrothermal solutions with the carbonate host rock which occurred earlier than silicification. This stage formed decalcification/sanding and generated the host rocks which is more suitable for mineralization. Average of gold and associated base metals' mineralization in this stage is very low (< 100 ppb) and close to the average of host rocks (Fig. 8). The small amounts of sulfides which are the first stage of sulphidization were formed at this stage. They consist of large euhedral pyrite grains which were mostly oxidized (Fig. 7A). Threshold values for Au in the host rocks are equal to Au medians in these rocks which are 0.22 ppm, 74 ppb and 0.12 ppm for calcschists – marbles, schists and dolomitic rocks, respectively.

Stage 2 (main hypogene mineralization): This stage formed the

Table 1
Results of sample analysis for Au.

No-Sample	Au (ppb)	No-Sample	Au (ppb)	No-Sample	Au (ppb)	No-Sample	Au (ppb)	No-Sample	Au (ppb)	No-Sample	Au (ppb)
IR25036	899	IR25655	34	IR25682	312	IR25709	560	IR25736	92	88-SMH-102	5880
IR25037	3914	IR25656	129	IR25683	74	IR25710	1332	IR25737	18	88-SMH-104	290
IR25038	409	IR25657	28	IR25684	195	IR25711	437	IR25738	57	88-SMH-108	2
IR25039	1349	IR25658	5	IR25685	14	IR25712	882	IR26219	321	88-SMH-110	62
IR25040	403	IR25659	483	IR25686	13	IR25713	637	88-SMH-151	5.9	88-SMH-111	8.5
IR25041	339	IR25660	417	IR25687	12	IR25714	75	88-SMH-152	2.1	88-SMH-112	1630
IR25168	49	IR25661	30	IR25688	36	IR25715	70	88-SMH-153	39	88-SMH-114	330
IR25169	142	IR25662	629	IR25689	226	IR25716	226	88-SMH-155	150	88-SMH-116	61
IR25170	111	IR25663	172	IR25690	121	IR25717	35	88-SMH-157	3.5	88-SMH-118	810
IR25171	3	IR25664	137	IR25691	58	IR25718	253	88-SMH-158	200	88-SMH-120	910
IR25499	284	IR25665	384	IR25692	174	IR25719	38	88-SMH-159	3.6	88-SMH-121	92
IR25500	96	IR25666	1071	IR25693	74	IR25720	4	88-SMH-160	3.5	88-SMH-123	1750
IR25640	178	IR25667	26	IR25694	271	IR25721	5	88-SMH-161	2.1	88-SMH-124	1580
IR25641	301	IR25668	219	IR25695	281	IR25722	16	88-SMH-162	3	88-SMH-126	670
IR25642	404	IR25669	118	IR25696	311	IR25723	1508	88-SMH-163	2	88-SMH-129	83
IR25643	20	IR25670	111	IR25697	642	IR25724	168	88-SMH-164	9.5	88-SMH-132	300
IR25644	56	IR25671	356	IR25698	93	IR25725	148	88-SMH-165	33	88-SMH-133	240
IR25645	124	IR25672	474	IR25699	114	IR25726	360	88-SMH-166	5.8	88-SMH-134	5.9
IR25646	2322	IR25673	243	IR25700	53	IR25727	358	88-SMH-167	1.2	88-SMH-135	180
IR25647	113	IR25674	54	IR25701	170	IR25728	273	88-SMH-168	170	88-SMH-136	1300
IR25648	900	IR25675	6	IR25702	82	IR25729	126	88-SMH-169	4.6	88-SMH-137	100
IR25649	72	IR25676	212	IR25703	801	IR25730	22	88-SMH-170	41	88-SMH-138	27
IR25650	224	IR25677	1125	IR25704	271	IR25731	46	88-SMH-171	840	88-SMH-139	1320
IR25651	188	IR25678	78	IR25705	419	IR25732	38	88-SMH-172	13	88-SMH-140	310
IR25652	90	IR25679	480	IR25706	98	IR25733	67	88-SMH-173	8.4	88-SMH-147	3.2
IR25653	71	IR25680	241	IR25707	610	IR25734	67	88-SMH-174	2.8	88-SMH-149	1.6
IR25654	41	IR25681	3033	IR25708	547	IR25735	51	88-SMH-175	3.9	88-SMH-150	3.6
87-SHM-9	210	87-SHM-8	1330								

main hypogene mineralization phase that is related to influx of hydrothermal fluids in the fractured zones with high permeability. This stage consists of three phases, as depicted in Fig. 8. The phase A is associated with the first stage of silicification (jasperoids) and sulfide mineralization which is mainly observed as fine grain disseminated sulfides within quartz veins and massive sulfides in the surrounding areas of quartz veins (Fig. 4C and D). Therefore, more sulfides of this phase are associated with carbonate alteration, especially dolomitization (Fig. 9). The quartz has been formed as veins within the fractures as well as peripheral veins within the host rock. The veins were mainly replaced in the NE-SW fractures. therefore, they cut the schistosity and foliation of the host rock (Fig. 9A and B). The size of the sulfides in this phase varies from amorphous to coarse grains. The volume of sulfides in this phase varies from less than 1 percent within jasperoids, which mainly contains pyrite, arsenian pyrite, and more than 5 percent within the host rock (Fig. 9) containing base metal sulfides such as galena, sphalerite and chalcopyrite. Intergrowth of pyrite with chalcopyrite, galena with sphalerite and galena with chalcopyrite at this phase showed that mineralization of base metals occurred simultaneously. The average grade of gold mineralization in this phase is relatively low (100–400 ppb). Silver in the deposit occurs in low quantities in Galena.

In contrast, phase B is resulted from the filling of joints, cavities, stockworks of phase A and replacement of host rocks by bright silicic alteration as microcrystalline quartz and fine grained sulfides (Fig. 10A). In fact, the second stage mineralization is another phase of silicic alteration as crosscutting veins and hydrothermal breccias in silicified zone. This phase was accompanied by deposition of further sulfide minerals. Formation of this phase (B) occurred later than phase A but there are some evidences of simultaneous formation (Fig. 10). The most important feature of this phase is hydrothermal breccias development that is composed by angular fragments from phase A in a matrix of quartz and sulfide minerals (Fig. 5A and B). This stage plays an important role for mineralization because of open space filling in fractures, joints and breccia zones. The volume of quartz in this phase is less than the previous phase but the ratio of its sulfide to quartz is higher than the phase A. The content of its sulfide varies between 1% and 2% including pyrite, arsenian pyrite, stibnite and minor amounts of

sulfosalts such as tetrahedrite and tennantite (Fig. 12). Stibnite mineralization mostly occurs in this phase. Minerals such as tennantite, gold, electrum and solid solution of gold within arsenian pyrite were distinguished by mineralographical studies. The value of gold mineralization in this phase is from 400 to 1000 ppb.

During late phase (C) of the hydrothermal mineralization, arsenic sulfides were deposited with large amounts of barite. This phase follows the previous phase (B) and is formed by filling fractures and voids (Fig. 11). At this phase, there is no evidence of hydrothermal brecciation however, there are some signs of decreasing pressure and depositional fluids (Fig. 11). Silicic alteration is very low in this phase and sulfides mostly consist of realgar and orpiment. Separation of quartz and sulfide is obvious in this phase (Fig. 11B). The grade range of gold mineralization in this phase is higher than 1000 ppb because supergene has the most influence on it. The last phase of mineralization is characterized by presence of large crystals of blade barite which shows boiling process. This phase was formed in low temperature which could be the product of hot water circulation in epithermal system.

The last stage (III) or post mineralization in this system (Phase D) is related to the oxidation process. Oxidation in the Arabshah deposit has more than 30 m depth. This process plays a significant role in gold enrichment. As a result, this process causes releasing of gold in the form of inclusion or solid solution from sulfides. The oxidation in this section consists of two parts: 1-oxidation by acid leaching and 2-supergene process. The main products of these processes are oxide minerals such as hematite, goethite, pyrolusite, malachite, azurite, chalcocite, covellite, smithsonite, cerussite, rhodochrosite, siderite, ankerite, gypsum and anhydrite.

The geochemical studies indicated that there is a strong correlation between gold and Hg, As, Ag and Sb (Heidari, 2013). This correlation shows a typical epithermal gold mineralization system. The presence of base metals and accumulation of heavy minerals such as stibnite and cinnabar may address a low-sulfidation epithermal gold mineralization.
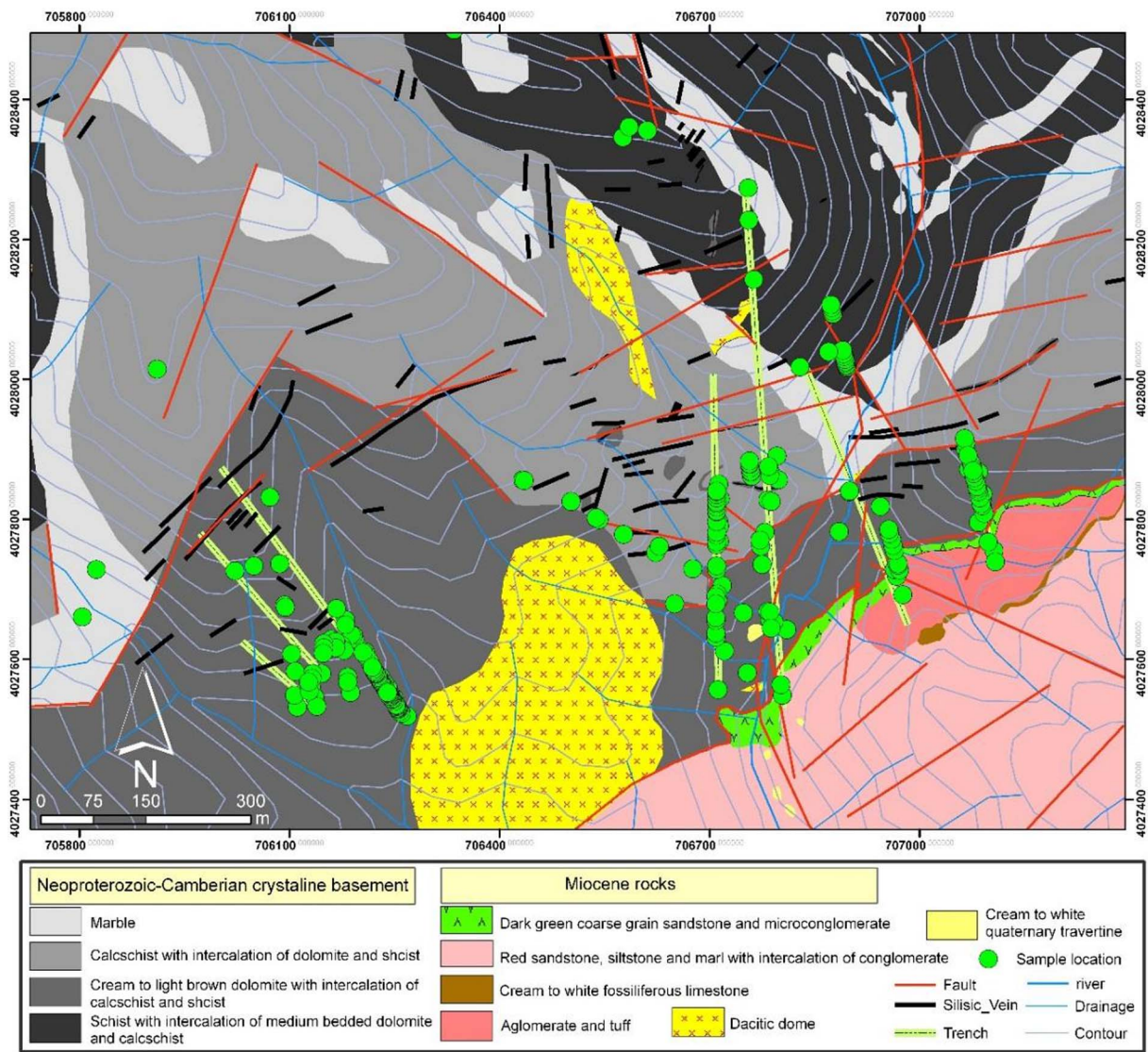
Fig. 12. Geology of Arabshah deposit showing the location map of lithogeochemical samples.
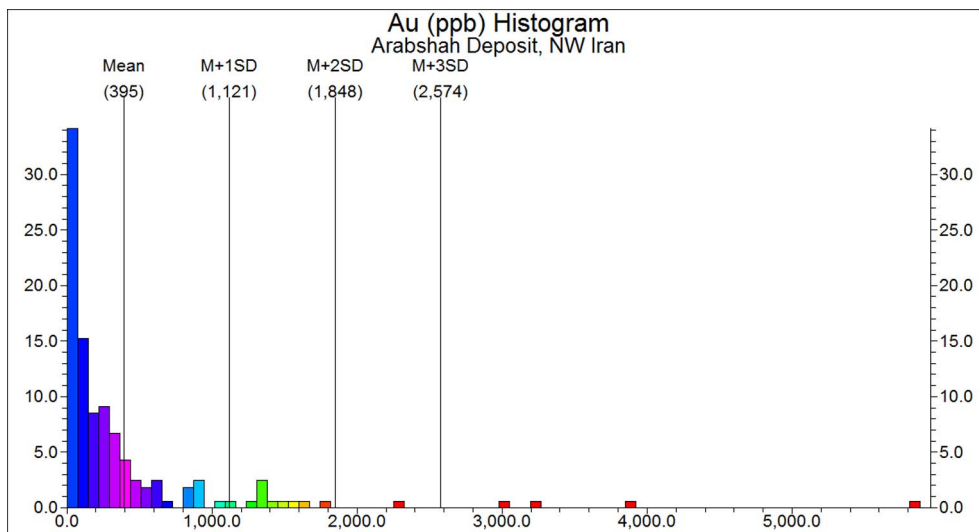

Fig. 13. Au histogram for the lithogeochemical samples.

Gaussian Without Nugget

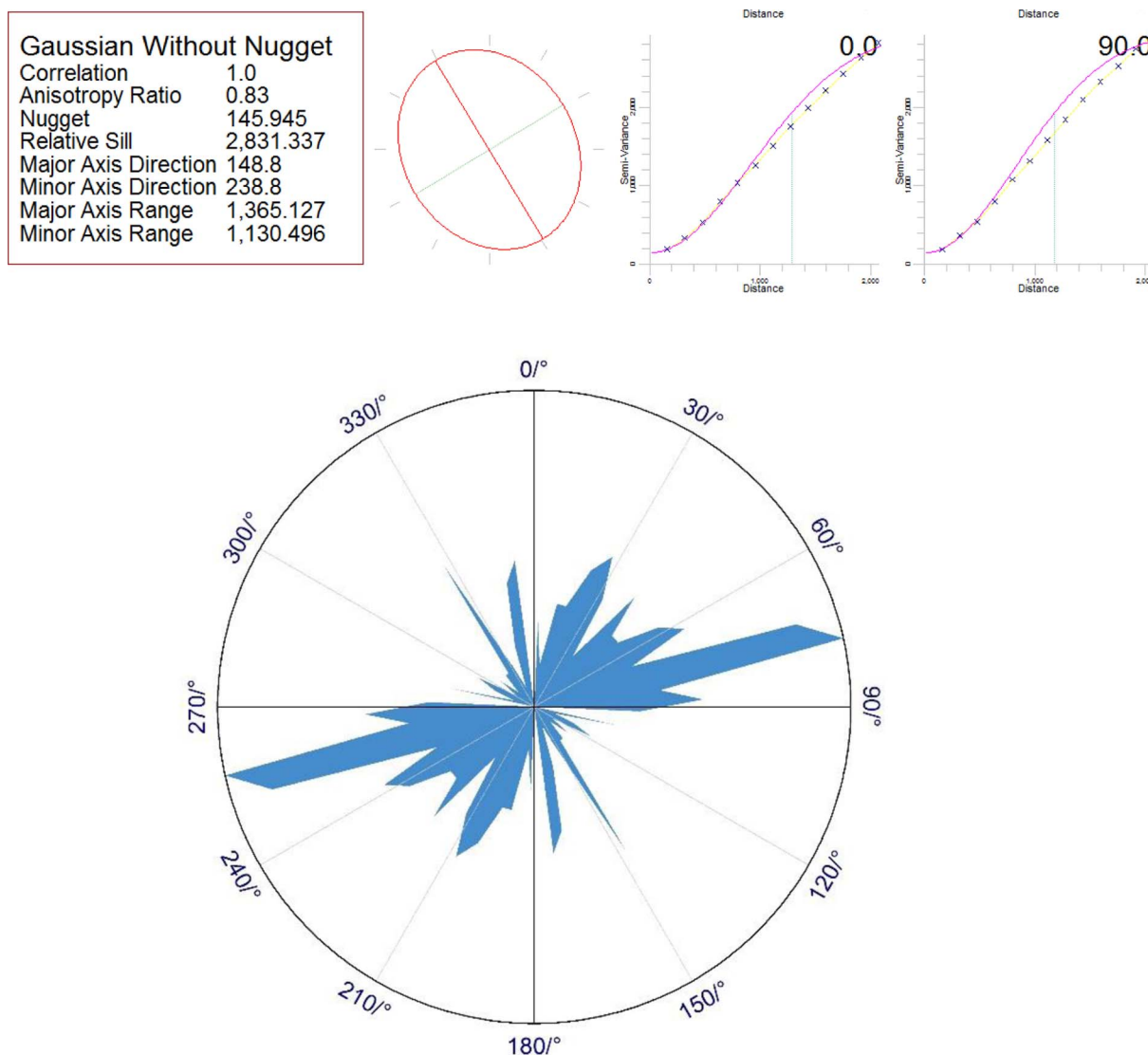|	
Correlation	1.0
Anisotropy Ratio	0.83
Nugget	145.945
Relative Sill	2,831.337
Major Axis Direction	148.8
Minor Axis Direction	238.8
Major Axis Range	1,365.127
Minor Axis Range	1,130.496

Fig. 14. Experimental variograms for Au and its anisotropic ellipsoid with rose diagram of area's structures.

Table 2
Factors obtained by the factor analysis.

Rotated Component Matrix[a]		
	Component	
	1	2
ln Au	.388	.748
ln Hg	.756	.286
ln As	.764	−.006
ln Sb	.818	−.087
ln Ag	.779	.290
ln Cu	.830	.113
ln Pb	.798	−.181
ln Zn	.782	−.455
ln Mn	.190	−.694
ln Ba	.752	.018

Extraction Method: Principal Component Analysis.
Rotation Method: Varimax with Kaiser Normalization.
  [a] Rotation converged in 3 iterations.

4. Discussion and results

4.1. Assay quality assurance and quality control

Sampling is an important part in geochemical exploration for different stages of mineral exploration and economic geology. The optimum sampling strategy should be based on geochemical methods followed by the field geology, variety of sampling, sample preparation and analytical technique. The calculation of reproducibility (precision) allows us to quantify variation of sampling and laboratory analysis, which is an integral part of the geochemical data interpretation. Consequently, any mistake in sampling and sample preparation may influence the results of the analysis (Thompson and Howarth, 1978; Fletcher, 1981; Demetriades, 2014; Yasrebi, 2014).

A total number of 164 lithogeochemical samples were analyzed by A.A.S. and ICP-MS for Au and related 44 elements by ALS Chemex (ALS Canada Ltd) laboratory (Table 1). The lithogeochemical samples were occupied by silicic veins (Fig. 12). Detection limits for Au, Ag, and Hg are 1 ppb, 0.5 ppm and 1 ppm, respectively. Moreover, 10 randomized samples for Au determination were selected and analyzed for quality assurance and quality control purposes using F-Distribution (Fisher) and T-student tests (Davis, 2002).
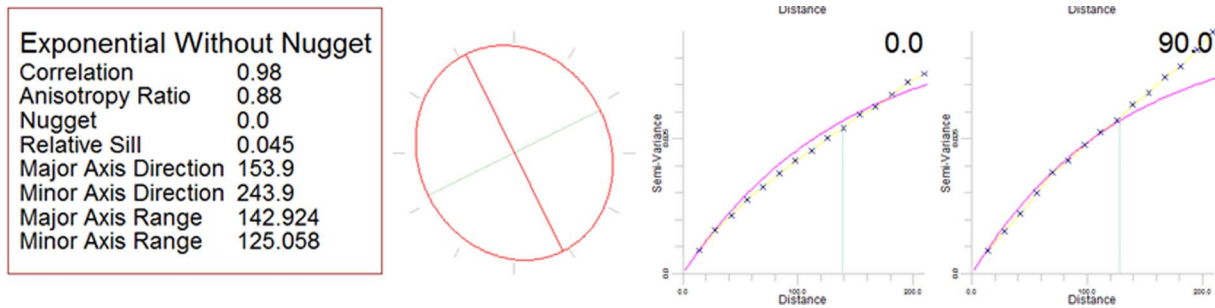
Fig. 15. Experimental variograms for F2 (Au and Mn) with its anisotropic ellipsoid.

4.1.1. Comparison of geochemical data variances via F-distribution (Fisher) test

F-distribution test is used to determined variances equality of duplicated samples (e.g., geochemical data). This is the theoretical distribution of values which are expected by randomly sampling from a normal population and calculating, for all possible pairs of sample variances and the ratio as follows (Deutsch and Journel, 1998; Davis, 2002; Yasrebi, 2014):

$$F = \frac{S_1^2}{S_2^2} \quad S_1 \geqslant S_2 \tag{2}$$

where F, S_1^2 and S_2^2 represent F-distribution or continuous probability distribution and variances for pair of samples (($S_1^2 = 329369.8222$ and $S_2^2 = 176592.5444$). The variances of double samples vary if the number of observations used in their calculation is small. Therefore, the shape of the F-distribution is expected to change with changes in terms of samples amounts.

The F-distribution has two degrees of freedom equal to n_1-1 and n_2-1 represent the number of observations equal to 9. Fisher indicated that significance level, 1–α (α: probability value) is calculated in the cases of one-tailed and two-tailed distributions depending on the defining alternative hypothesis. The hypotheses are as follows (Fisher and Tippett, 1928):

Null hypothesis: $H_0: S_1^2 = S_2^2 \tag{3}$

Alternative hypothesis: $H_1: S_1^2 \neq S_1^2 \tag{4}$

Based on the F-test, $F(9,9) \approx 1.86$ which is < 3.18 with respect to the confidence level of 95% ($a = 0.05$). As a result, the Null hypothesis is acceptable representing that two variances obtained from the paired samples are almost equal to each other (Emery, 2012).

4.1.2. Comparison of geochemical data means via paired T-student test

A T-student test is used to compare means of two populations. The paired sample T-tests typically include a sample of matched pairs of similar units, e.g., Au (ppb) in this study, or one group of units that has been tested twice (e.g., Davis, 2002). There are null and alternative hypothesizes that null hypothesis shows no difference between mean values like to Fisher test. The procedure of the T-student test is described as follows:

- Calculate the difference between the two observations on each pair as follow:

$$d_i = y_i - x_i \tag{5}$$

- Calculate the mean difference of the pair samples based on their grades ($\bar{d}$). The means of grades for the paired samples are 414 ppb and 610.4 ppb so $\bar{d}$ is 489.5 ppb.
- Standard error ($SE(\bar{d})$) of the mean difference was calculated by the following formulas:

$$S_d = Sd_1^2 - Sd_2^2 \tag{6}$$

$$SE(\bar{d}) = \frac{S_d}{\sqrt{\bar{n}}} \tag{7}$$

where S_d difference between standard deviations of the pair samples ((Sd_1^2 and Sd_2^2). Furthermore, $\bar{n}$ is equal to 2 because there is a pair of samples.

- Calculate the T-test statistic under the null hypothesis, this statistic follows a T-distribution with n – 1 degrees of freedom by following equation:

$$T = \frac{\bar{d}}{SE(d)\sqrt{\frac{2}{n}}} \tag{8}$$

where n is number of paired samples which is 10 in the studied area.

- Finally, the calculated T compared to standard T from related statistical table with n-1 freedom degree. This table will give a critical value for T (P-value) which is defined as the smallest level of significance at which the null hypothesis would be rejected for a specific test, for the paired T-test (Davis, 2002). The calculated T is −0.87358 based on the Eq. (8) and also, the P-value is 1.393 in the 95% confidence level which indicates that the null hypothesis is again acceptable. Therefore, the mean values of the paired samples are equal (Davis, 2002).

Based on the T-student and Fisher tests, there is no significant difference between results obtained via raw and controlling samples giving an analytical accuracy in this deposit.

4.2. Statistical and geostatistical analysis for lithogeochemical data

Classical statistical analysis shows that Au mean and median values are 395 ppb and 149 ppb, respectively. The Au histogram is not normal which reveals that the Au median value can be assumed as threshold value (Davis, 2002; Fig. 13). Moreover, the different thresholds for various anomalies can be calculated based on summation of median (MD) and standard deviation (SD). The threshold values for low (MD + SD), medium (MD + 2SD) and high (MD + 3SD) intensive anomalous parts are 875 ppb, 1601 ppb and 2327 ppb, respectively.

Au geostatistical analysis was carried out for creation of Au geochemical map. Based on the analysis, anisotropic ellipsoid with the experimental variograms were generated as depicted in Fig. 14. The main directions of this ellipsoid are similar to the structural directions in its rose diagram as shown in Fig. 14. As a result, the gold mineralization has a direct relationship with faults especially with the NE-SW and NW-SE trends due to the anisotropic ellipsoid which is similar to Geynardjeh-Chahartagh NW-SE thrust fault in the study area and also, the NE-SW strike-slip fault in the Arabshah deposit. The mineralized silicic veins/veinlets have the NE-SW trend in the area which is correlated with the rose diagram and anisotropic ellipsoid (Fig. 14).

**Fig. 16.** S-A log-log plots for Au (a) and F2 (b).
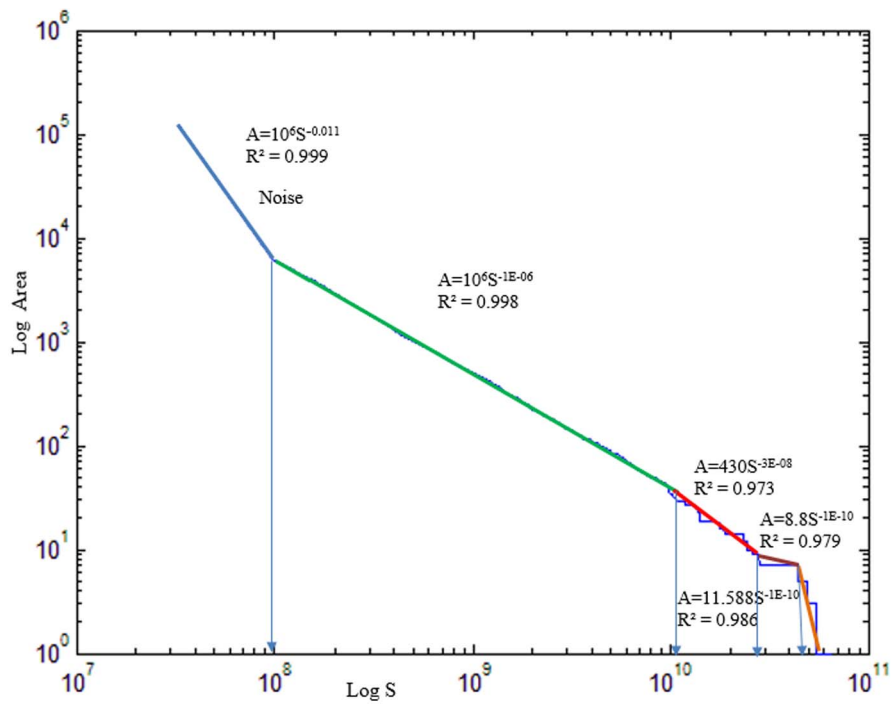

(a)
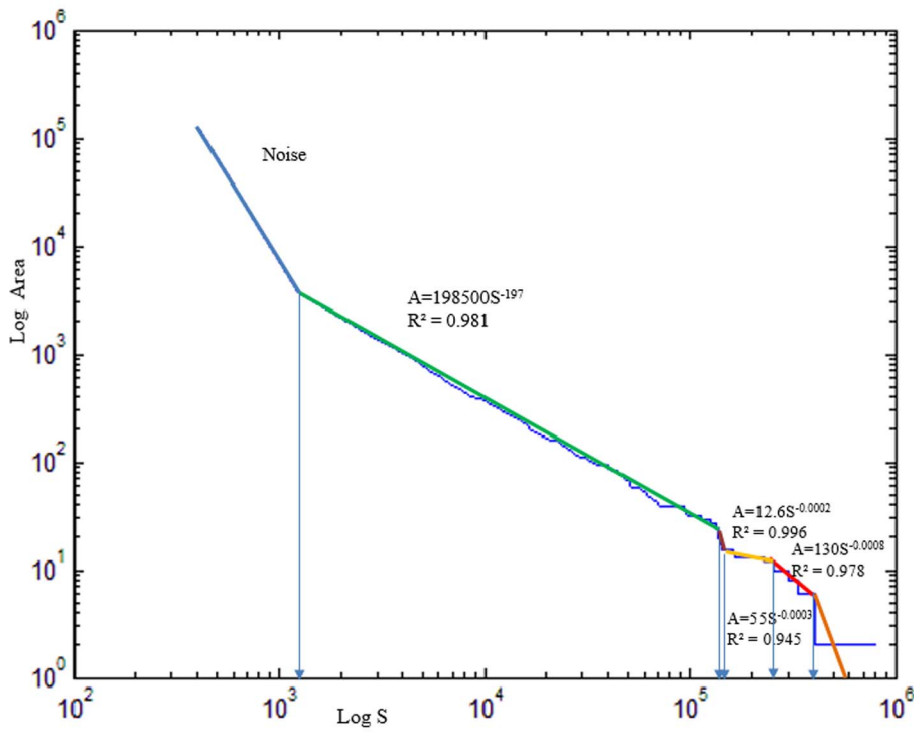
(b)

4.3. Application of factor analysis

The factor analysis was performed in the log-transformed litho-geochemical data. The factor analysis was applied on 10 elements related to gold mineralization. The elements were classified in two factors

using SPSS software to the following groups (Table 2):

(1) Hg, As, Sb, Ag, Cu, Pb, Zn and Ba and (2) Au and Mn. The factor 2 (F2) consists of Au and Mn is important in the area for mineralization which is used for the S-A fractal analysis. For this aim, its variograms and anisotropic ellipsoid were built up as depicted in Fig. 15. The major
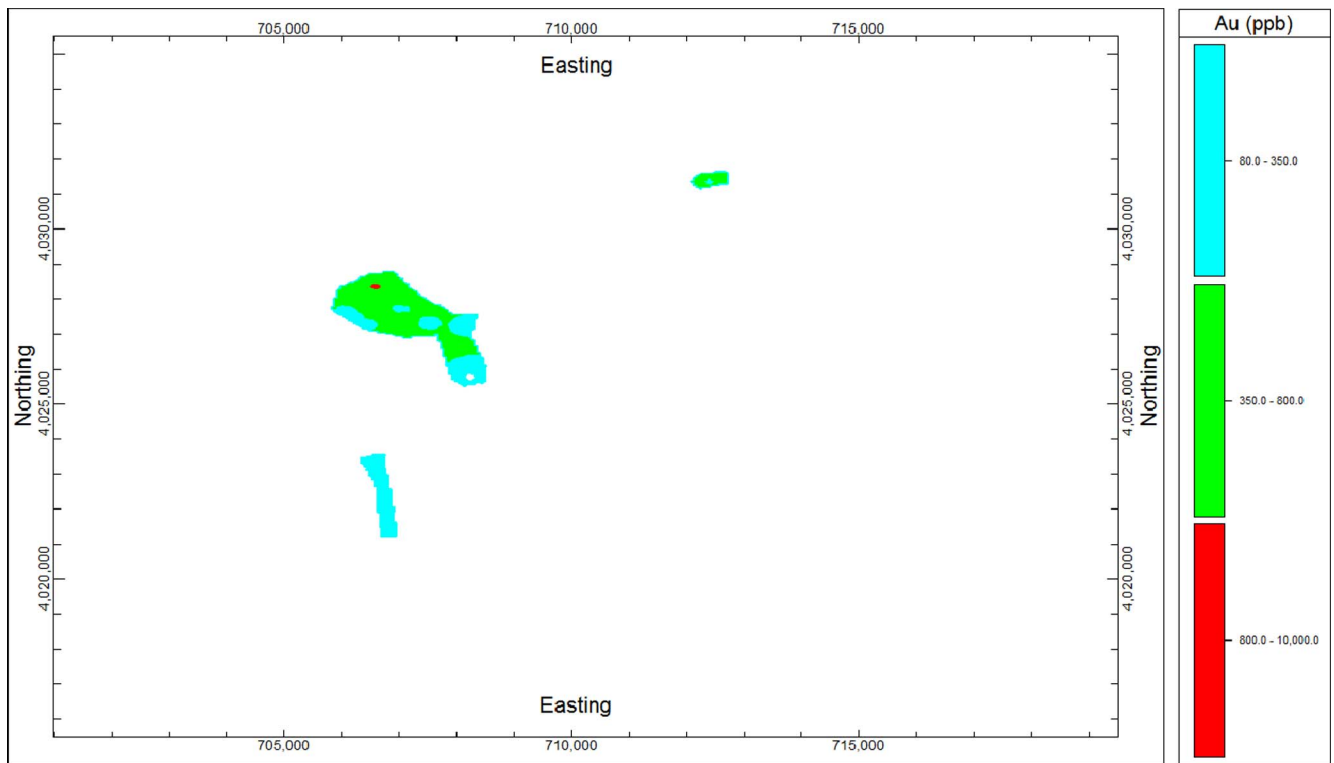
(a)
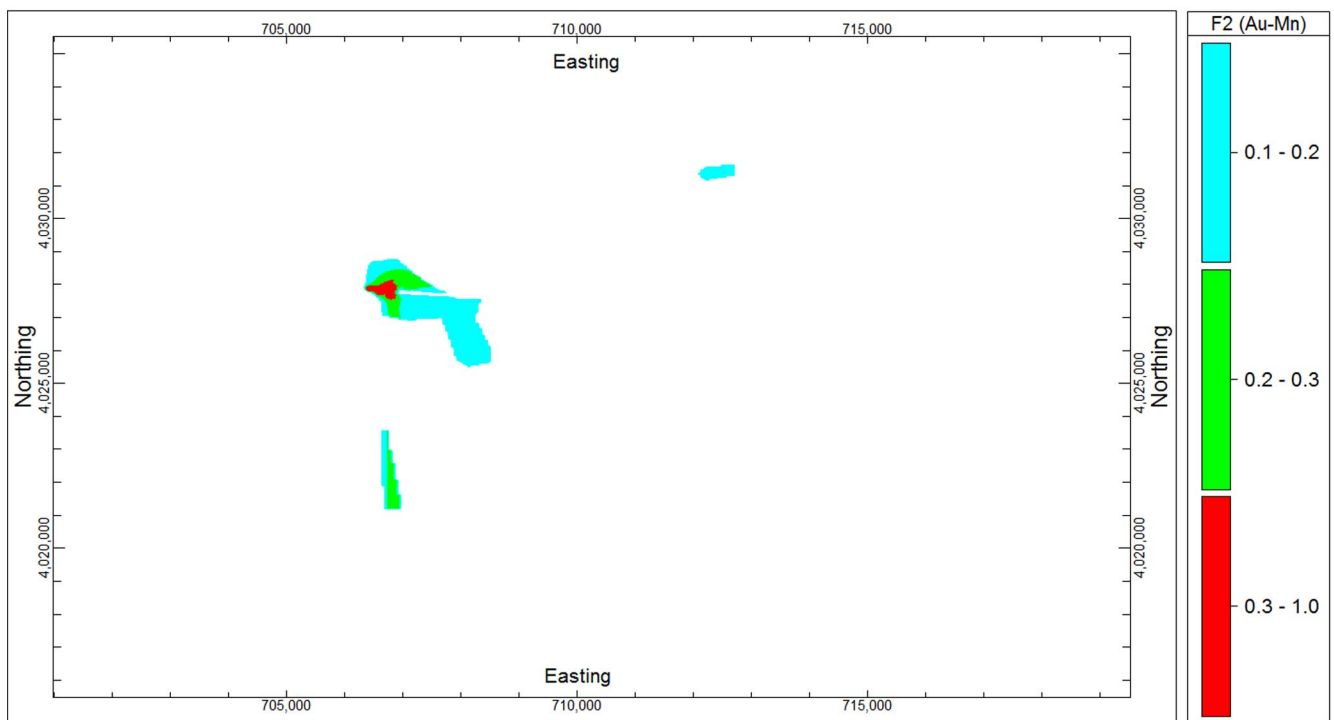
(b)

Fig. 17. a) Au and b) F2 (Au-Mn) distribution maps based on the S-A fractal modelling.

directions of F2 are correlated with main direction of the NE-SW strike slip and Geynardjeh-Chahartagh NW-SE thrust faults and structures in this area such as Au anisotropic ellipsoid (Fig. 15).

4.4. Application of S-A fractal modelling

Lithogeochemical maps were created with OK (Ordinary Kriging) estimation method by RockWorks software package. The study area was gridded by 10 m × 10 m cells due to distance of sampling and silicic
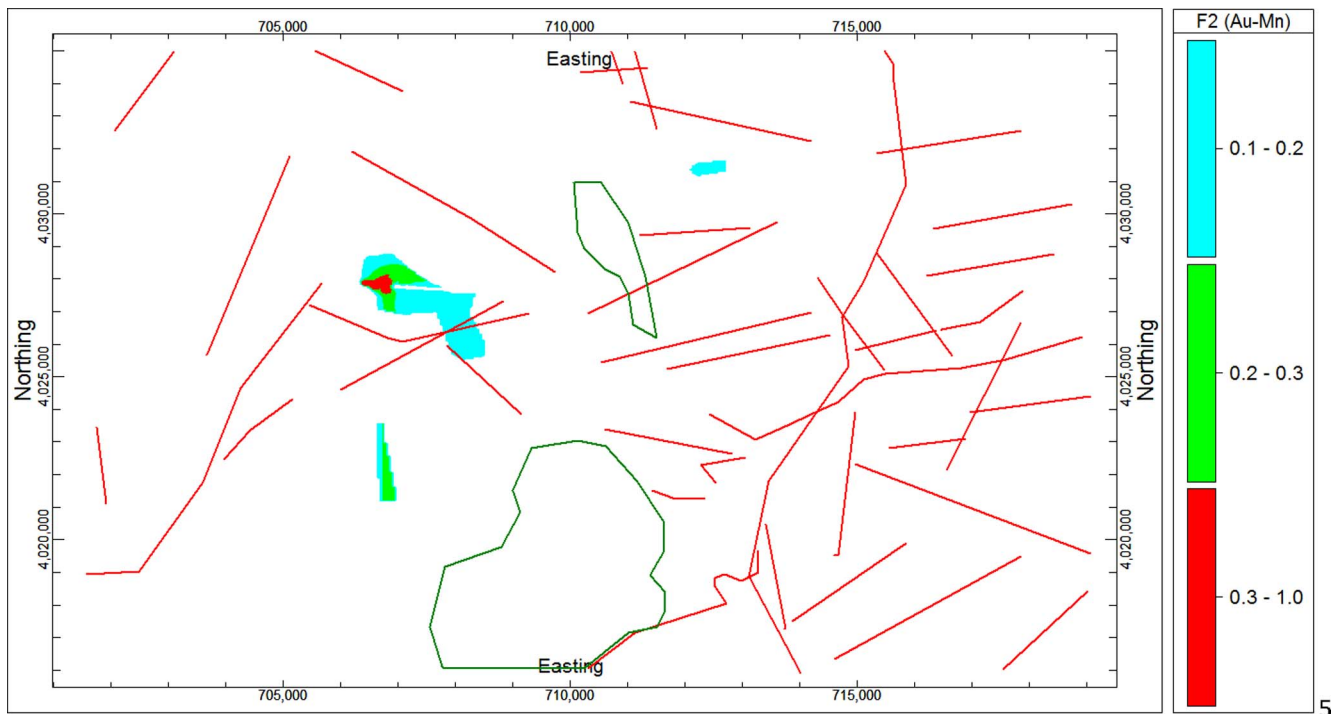
Fig. 18. Comparison among faults (red lines), intrusive rocks (green polygons) and F2 populations. (For interpretation of the references to colour in this figure legend, the reader is referred to the web version of this article.)

veins (David, 1970). The Au and F2 geochemical maps were utilized as input data to the FPSA software. The FPSA software was designed for S-A data processing and generation of log-log plots (Afzal et al., 2013b). The power spectrum (PS) was calculated for the 2D elemental distributions utilizing 2D Fourier transformation. Logarithmic values of PS versus area (A) were plotted with fitting straight line segments as illustrated in Fig. 16.

Results demonstrate that the spectrum for Au and F2 have five different power-law relationships as depicted in their log-log plots. The multifractal properties may imply the relationship between Au mineralization and its related factor with geological processes. The components with relatively higher frequencies (lower values of PS) give larger slopes $(2/\beta > 1)$, implying that these components indicate multifractal nature, while the background with lower frequencies (higher values of PS) may related to non-fractals or bi-fractals (Afzal et al., 2013b; Zuo et al., 2013).

There is a sudden change in decrease rate of the areas enclosed by high values of power spectrum as depicted in Fig. 16. According to these thresholds values, filters were designed for delineation of anomalous parts from background. The first thresholds of PS_0 for Au and F2 are 10^8 (log PS = 8) and 1258.92 (log PS = 3.1), respectively. Furthermore, second threshold values for Au and F2 of PS_0 are 10^{10} (log PS = 10) and 158489.31 (log PS = 5.2) were derived via S-A log-log plot, respectively. Moreover, Au and F2 third thresholds are 31622776601.68 (log PS = 10.5) and 316227.77 (log PS = 5.5) and also, last thresholds for Au and F2 are equal to 63095734448.02 (log PS = 10.8) and 501187.23 (log PS = 5.7) respectively.

The left-hand and right-hand lines represent noise and geochemical background and the middle-lines show geochemical anomalies (Zuo et al., 2013). The PS values higher than $10^{10.8}$ and 501187.23 are the background filter for Au and F1-5. Other filters defined for anomalies of Au and F1-5 in PS ranges 10^8-$10^{10.8}$ and 1258.92-501187.23 show different mineralization stages. Inverse fast Fourier transformation (IFFT) was useful in these filters to convert the decomposed components back to the space domain.

Based on the model, background with Au grades < 80 ppb and F2 values lower than 0.1 is correlated with pre-mineralization stage.

However, Au concentrations in the first phase (A) of the second stage varies between 80 and 350 ppb. Second phase of this stage has Au values between 350 and 800 ppb, which are situated in the northern and central parts of the Arabshah deposit (Fig. 17). Au concentrations > 800 ppb represent final stage of Au mineralization associated with C and D phases which occur in the central part of the area, as depicted in Fig. 17. Furthermore, this stage comprises F2 > 0.3 known as an enriched zone for Au and Mn with a good correlation with Au values > 800 ppb. First populations of the log-log plots with Au values < 80 ppb and F2 < 0.1 indicate the background (pre-mineralization).

4.5. Correlation between geological and fractal modelling

Comparison between faults and rock types (Heidari, 2013; Heidari et al., 2013, 2015) obtained from the geological modelling was carried out. This reveals that the main mineralized stages obtained by the fractal modeling and factor analysis have proper correlation with faults and intrusive rocks, as shown in Fig. 18. The intrusive rocks are located in the proximity of the main Au and F2 anomalies in the central and southern parts of the Arabshah deposit. These rocks can be a possible source of heating or hydrothermal fluids. Based on the results obtained by the geological data and fractal modeling, three mineralization stages have been identified:

1. Extensive acid leaching on the host limestone was followed by pervasive silicification associated with a first phase of sulfide mineralization with Au grades between 80 and 350 ppb and F2 values between 0.1 and 0.2.
2. Second stage mineralization and silicification were accompanied by deposition of further sulfide minerals. There are Au and F2 values of 350–800 ppb and 0.2–0.3, respectively, in this stage.
3. During the late stage mineralization, arsenic sulfides were formed and cinnabar was deposited with large amounts of barite with Au and F2 values higher than 800 ppb and 0.3, respectively.

5. Conclusions

Combination between the S-A fractal modeling and factor analysis for geochemical data with respect to geological evidences in the Arabshah deposit demonstrated that there are three stages for Au mineralization. Based on the fractal modeling and geological data, main mineralization stage occurs in the central part of the area which is associated with the NE-SW and NW-SE trending faults and altered intrusive rocks. There are F2 (Au-Mn) and Au concentrations greater than 0.3 and 800 ppb, respectively. This indicates that there is a major stage of gold mineralization. The main mineralization phase obtained by the fractal model has correlation with C and D phases derived via geological data including arsenian pyrites, realgar, orpiment and oxidized sulfides. Pre-mineralization (first stage) has Au content lower than 80 ppb and F2 value less than 0.1. This stage is characterized with decalcification and acid leaching. First part of the second stage (phase A) with Au grades between 80 and 350 ppb is situated in the northern, central and southeastern parts of the study area. This phase mostly contains base metal sulfides associated with trace pyrites and arsenian pyrites. Second mineralization stage contains Au and F2 values of 350–800 ppb and 0.2–0.3, respectively, with association of silicification and further sulfide minerals' deposition.

Acknowledgment

References

Afzal, P., Dadashzadeh Ahari, H., Rashidnejad Omran, N., Aliyari, F., 2013a. Delineation of gold mineralized zones using concentration-volume fractal model in Qolqoleh gold deposit, NW Iran. Ore Geol. Rev. 55, 125–133.

Afzal, P., Fadakar Alghalandis, Y., Khakzad, A., Moarefvand, P., Rashidnejad Omran, N., 2011. Delineation of mineralization zones in porphyry Cu deposits by fractal concentration–volume modeling. J. Geochem. Explor. 108, 220–232.

Afzal, P., Fadakar Alghalandis, Y., Moarefvand, P., Rashidnejad Omran, N., Asadi Haroni, H., 2012. Application of power-spectrum-volume fractal method for detecting hypogene, supergene enrichment, leached and barren zones in Kahang Cu porphyry deposit, Central Iran. J. Geochem. Explor. 112, 131–138.

Afzal, P., Harati, H., Fadakar Alghalandis, Y., Yasrebi, A.B., 2013b. Application of spectrum–area fractal model to identify of geochemical anomalies based on soil data in Kahang porphyry-type Cu deposit, Iran. Chemie der Erde 73, 533–543.

Agard, P., Omrani, J., Jolivet, L., Whtechurch, H., Vrielynck, B., Spakman, W., Monie, P., Meyer, B., Wortel, R., 2011. Zagros orogeny: a subduction-dominated process, Geol. Mag., 148, 692–725.

Agterberg, F.P., 1995. Multifractal modeling of the sizes and grades of giant and supergiant deposits. Int. Geol. Rev. 37, 1–8.

Alavi, M., 1994. Tectonics of the Zagros orogenic belt of Iran: new data and interpretations. Tectonophysics 229, 211–238.

Alavi, M., 2004. Regional stratigraphy of the Zagros fold-thrust belt of Iran and its pro foreland evolution. Am. J. Sci. 304, 1–20.

Ali, K.h., Cheng, Q., Zhijun, C., 2007. Multifractal power spectrum and singularity analysis for modelling stream sediment geochemical distribution patterns to identify anomalies related to gold mineralization in Yunnan Province, South China. Geochem. Explor. Environ. Anal. 7, 293–301.

Allen, M.B., Blanc, E.J.P., Walker, R., Jackson, J., Talebian, M., Ghassemi, M.R., 2006. Contrasting styles of convergence in the Arabia-Eurasia collision: why escape tectonics does not occur in Iran. Geol. Soc. Am. Spec. Pap. 409, 579–589.

Asadi, H.H., Voncken, J.H.L., Hale, M., 1999. Invisible gold at Zarshuran, Iran. Econ. Geol. Soc. Econ. Geol. 94, 1367–1374.

Asadi, H.H., Voncken, J.H.L., Kühnel, R.A., Hale, M., 2000. Petrography, mineralogy and geochemistry of the Zarshouran Carlin-like gold deposit, northwest Iran. Mineral. Deposita 35, 656–671.

Berberian, M., King, G.C.P., 1981. Toward a paleogeography and tectonic evolution of Iran. Can. J. Earth Sci. 18, 210–265.

Berger, B.R., 1986. Descriptive model of carbonate-hosted Au-Ag. In: Cox, D.P., Singer, D.A., (Eds.), Mineral deposit models: U.S. Geological Survey Bulletin 1693, p. 175.

Berger, B.R., Bagby, W.C., 1991. The geology and origin of Carlin type deposit. In: Foster, R.P., (Ed.), Gold metallogeny and exploration. Blackie, Glasgow, pp. 210 ± 248.

Bolviken, B., Stokke, P.R., Feder, J., Jossang, T., 1992. The fractal nature of geochemical landscapes. J. Geochem. Explor. 43, 91–109.

Bonini, M., Corti, G., Sokoutis, D., Vannucci, G., Gasperini, P., Cloetingh, S., 2003. Insights from scaled analogue modelling into the seismotectonics of the Iranian region. Tectonophysics 376, 137–149.

Carranza, E.J.M., 2009. Controls on mineral deposit occurrence inferred from analysis of their spatial pattern and spatial association with geological features. Ore Geol. Rev. 35, 388–400.

Carranza, E.J.M., Sadeghi, M., 2012. Primary geochemical characteristics of mineral deposits—implications for exploration. Ore Geol. Rev. 45, 1–4.

Carranza, E.J.M., Sadeghi, M., Billay, A., 2015. Predictive mapping of prospectivity for orogenic gold, Giyani greenstone belt (South Africa). Ore Geol. Rev. 71, 703–718.

Cheng, Q., Agterberg, F.P., 2009. Singularity analysis of ore-mineral and toxic trace elements in stream sediments. Comput. Geosci. 35 (2), 234–244.

Cheng, Q., Xu, Y., Grunsky, E., 1999. Integrated spatial and spectral analysis for geochemical anomaly separation. In: Lippard, S.J., Naess, A., Sinding-Larsen, R., (Eds.), Proc. of the Conference of the International Association for Mathematical Geology, Trondheim, Norway, Vol. 1, 87–92.

Cheng, Q., 2000. Multifractal theory and geochemical element distribution pattern. Earth Sci.-J. China Univ. Geosci. 25 (3), 311–318.

Cheng, Q., 2004. A new model for quantifying anisotropic scale invariance and for decomposition of mixing patterns. Math. Geol. 36 (3), 345–360.

Cheng, Q., 2006. Multifractal modelling and spectrum analysis: methods and applications to gamma ray spectrometer data from southwestern Nova Scotia, Canada. Sci. China Ser. D: Earth Sci. 49 (3), 283–294.

Cheng, Q., 2007. Mapping singularities with stream sediment geochemical data for prediction of undiscovered mineral deposits in Gejiu, Yunnan Province, China. Ore Geol. Rev. 32, 314–324.

Cheng, Q., Agterberg, F.P., Ballantyne, S.B., 1994. The separartion of geochemical anomalies from background by fractal methods. J. Geochem. Explor. 51, 109–130.

Daliran, F., 2008. The carbonate rock-hosted epithermal gold deposit of Aghdarreh Takab geothermal field, NW Iran-hydrothermal alteration and mineralization. Mineral. Deposita 43, 383–404.

Daliran, F., Borg, G., Armstrong, R., Vennemann, T., Walther, J., Woodhead, J.D., 2009. Nonsulphide zinc deposits, Iran. The hypogene emplacement and supergene modification history of the Angouran zinc deposit, NW-Iran. Berichte zur Lagerstätten- und Rohstoffforschung 57, BGR Hannover, (75 pp.).

David, M., 1970. Geostatistical Ore Reserve Estimation. Elsevier, Amsterdam, pp. 283.

Davis, J.C., 2002. Statistics and Data Analysis in Geology, 3th ed. John Wiley & Sons Inc., New York.

Demetriades, A., 2014. Basic considerations: sampling, the key for a successful applied geochemical survey for mineral exploration and environmental purposes', Reference Module in Earth Systems and Environmental Sciences, Vol. 15: Analytical Geochemistry/Inorganic INSTR. Analysis, pp. 1–31.

Deutsch, C., Journel, A.G., 1998. GSLIB: Geostatistical Software Library and User's Guide, 2nd ed. Oxford University Press, New York.

Dill, H.G., 2011. The "chessboard" classification scheme of mineral deposits: mineralogy and geology from aluminum to zirconium. Earth-Sci. Rev. 100, 1–420.

Emery, X., 2012. Análisis estadístico de datos. Facultad de Ciencias, Físicas y Matemáticas, Universidad de Chile, 30 pp. (in Spanish).

Fisher, R.A., Tippett, L.H.C., 1928. Limiting forms of the frequency distribution of the largest or smallest member of a sample. Math. Proc. Cambridge Philos. Soc. 24 (2), 180–190.

Fletcher, W.K., 1981. Handbook of Exploration Geochemistry 1: Analytical Methods in Geochemical Exploration, in Govett, G.J.S. (Ed.): Elsevier, Amsterdam, pp. 25–46.

Fonoudi, M., Hariri, A., Babakhani, A., 1998. Geological map of Takab, 1:100,000, Sheet No 5462, GSI–Geological Survey of Iran.

Ghasemi, A., Talbot, C.J., 2006. A new tectonic scenario for the Sananda-Sirjan Zone (Iran). J. Asian Earth Sci. 26, 683–693.

Gilg, H.A., Boni, M., Balassone, G., Allen, C.R., Banks, D., Moore, F., 2005. Marble-hosted sulfide ores in the Anguran Zn-(Pb-Ag) deposit, NW Iran: interaction of sedimentary brines with a metamorphic core complex. Miner. Deposita 41, 1–16.

Glennie, K.W., 2000. Cretaceous tectonic evolution of Arabia's eastern plate margin: a tale of two oceans. Society for Sedimentary Geology (SEPM) Special Publication 69: 9–20.

Goldfarb R.J., Baker T., Dube B., Groves D.I., Hart C.J.R., Gosselin P., 2005, Distribution, Character, and Genesis of Gold Deposits in Metamorphic Terranes, in Economic Geology 100th Anniversary Volume, 407–450.

Goldfarb, R.J., Hart, C., Davis, G., Groves, D., 2007. East Asian gold: deciphering the anomaly of phanerozoic gold in Precambrian cratons. Econ. Geol. 102 (3), 341–347.

Groves, D.I., Vielreiche, R.M., Goldfarb, R.J., Condie, K.C., 2005. Controls on the heterogeneous distribution of mineral deposits through time, Mineral Deposits and Earth Evolution. Geol. Soc., London, Spec. Publ. 248, 71–101.

Ghalamghash, J., Babakhani, A., 1992. Geological map of Takht-e-Soleyman, 1:100,000, Sheet No 5463, GSI–Geological Survey of Iran.

GSI–Geological Survey of Iran, 2006, Geological map of Iran: Tehran, Geological Survey of Iran, 1 sheet, 1:2,500,000.

Gumiel, P., Sanderson, D.J., Arias, M., Roberts, S., Martín-Izard, A., 2010. Analysis of the fractal clustering of ore deposits in the Spanish Iberian Pyrite Belt. Ore Geol. Rev. 38, 307–318.

Hedenquist, J.W., Arribas, R.A., Gonzalez-Urien, E., 2000. Exploration for epithermal gold deposits. In: Hagemann, S.G. (Ed.), Gold in 2000. Reviews in Economic Geology, vol. 13, pp. 245–277.

Heidari S.M., 2013. Geology, geochronology, geological setting and source of Touzlar, Arabshah and Gozalbolagh gold occurences in Qorveh-Takab region, Unpublished PhD Thesis, Tarbiat Modares University, Tehran, Iran.

Heidari, S.M., Daliran, F., Paquette, J.L., Gasquet, D., 2015. Geology, timing, and genesis of the high sulfidation Au (–Cu) deposit of Touzlar, NW Iran. Ore Geol. Rev. 2 (65), 460–486.

Heidari, S.M., Ghaderi, M., Afzal, P., 2013. Delineating mineralized phases based on lithogeochemical data using multifractal model in Touzlar epithermal Au-Ag (Cu) deposit, NW Iran. Appl. Geochem. 31, 119–132.

Johnson, R.A., Wichern, D.W., 2002. Applied Multivariate Statistical Analysis, 5th ed.

Prentice Hall, New Jersey.

Jolliffe, I.T., 2002. Principal Component Analysis, 2nd ed. Springer, New York.

Karamsoltani, M., Emam Jomeh, A., Yarmohammadi, A., 2004. Geology and Exploration of Arabshah deposit (1:1000), SE of Takab. Report of Madan Zamin Exploration Consultant Engineers, p. 80 (in Persian).

Krumbein, W.C., Graybill, F.A., 1965. An Introduction to Statistical Models in Geology. McGraw-Hill, New York.

Li, C.J., Ma, T.H., Shi, J.F., 2003. Application of a fractal method relating concentration and distances for separation of geochemical anomalie from background. J. Geochem. Explor. 77, 167–175.

Mandelbrot, B.B., 1983. The Fractal Geometry of Nature. W. H. Freeman, San Fransisco.

Mehrabi, B., Yardley, B.W.D., Cann, J.R., 1999. Sediment-hosted disseminated gold mineralization at Zarshuran, NW Iran. Mineral. Deposita 34, 673–696.

Mohajjel, M., Fergusson, C.L., Sahandi, M.R., 2003. Cretaceous-Tertiary convergence and continental collision, Sanandaj-Sirjan zone, western Iran. J. Asian Earth Sci. 21, 397–412.

Muller, J., Kylander, M., Martinez-Cortizas, A., Wüst, R.A.J., Weiss, D., Blake, K., Coles, B., Garcia-Sanchez, R., 2008. The use of principle component analyses in characterizing trace and major elemental distribution in a 55 kyr peat deposit in tropical Australia: implications to paleoclimate. Geochim. Cosmochim. Acta 72, 449–463.

Nazarpour, A., Sadeghi, B., Sadeghi, M., 2015. Application of fractal models to characterization and evaluation of vertical distribution of geochemical data in Zarshuran gold deposit, NW Iran. J. Geochem. Explor. 148, 60–70.

Parsa, M., Maghsoudi, A., Yousefi, M., Sadeghi, M., 2016a. Multifractal analysis of stream sediment geochemical data: implications for hydrothermal nickel prospection in an arid terrain, eastern Iran. J. Afr. Earth Sci. http://dx.doi.org/10.1016/j.gexplo.2016.11.013.

Parsa, M., Maghsoudi, A., Yousefi, M., Carranza, E.J.M., 2016b. Multifractal interpolation and spectrum-area fractal modeling of stream sediment geochemical data: implications for mapping exploration targets. J. Afr. Earth Sci. http://dx.doi.org/10.1016/j.jafrearsci.2016.11.021.

Pirajno, F., 2009. Hydrothermal Processes and Mineral Systems. Springer, Berlin (1250 pp.).

Reimann, C., Filzmoser, P., Garrett, R.G., 2005. Background and threshold: critical comparison of methods of determination. Sci. Total Environ. 346, 1–16.

Richards, J.P., Wilkinson, D., Ullrich, T., 2006. Geology of the Sari Gunay epithermal gold deposit northwest Iran. Econ. Geol. 101, 1455–1496.

Robert, F., Brommecker, R., Bourne, B.T., Dobak, P. J., McEwan, C.J., Rowe, R. R., Zhou, X., 2007. Models and exploration methods for major gold deposit types. In: Milkereit, B., (Ed.), Proceedings of Exploration 07: Fifth Decennial International Conference on Mineral Exploration, pp. 691–711.

Sadeghi, B., Madani, N., Carranza, E.J.M., 2015. Combination of geostatistical simulation and fractal modeling for mineral resource classification. J. Geochem. Explor. 149, 59–73.

Shafiei, B., Haschke, M., Shahabpour, J., 2009. Recycling of orogenic arc crust triggers porphyry Cu mineralization in Kerman Cenozoic arc rocks southeastern Iran. Mineral. Deposita 44, 265–283.

Shamseddin Meigoony, M., Afzal, P., Gholinejad, M., Yasrebi, A.B., Sadeghi, B., 2014. Delineation of geochemical anomalies using factor analysis and multifractal modeling based on stream sediments data in Sarajeh 1:100,000 sheet, Central Iran. Arabian J. Geosci. 7, 5333–5343.

Sim, B.L., Agterberg, F.P., Beaudry, C., 1999. Determining the cutoff between background and relative base metal contamination levels using multifractal methods. Comput. Geosci. 25, 1023–1041.

Stockli, D., Hassanzadeh, J., Stockli, L., Axen, G., Walker, J.D., Terrence, T.J., 2004. Structural and geochronological evidence for Oligo-Miocene intra-arc low-angle detachment faulting in the Takab-Zanjan area, NW Iran. Geol. Soc. Amer. Abstr. Progr. 36 (5), 319.

Thompson, M., Howarth, S.R., 1978. A new approach to the estimation of analytical precision. J. Geochem. Explor. 9, 23–30.

Turcotte, D.L., 1986. A fractal approach to the relationship between ore grade and tonnage. Econ. Geol. 18, 1525–1532.

Verdel, C., Wernicke, B.P., Hassanzadeh, J., Guest, B., 2011. A Paleogene extensional arc flare-up in Iran. Tectonics 30 (TC3008), 19.

Wall, V.J., Graupner, T., Yantsen, V., Seltmann, R., and Hall, G.C., 2004, Muruntau, Uzbekistan: a giant thermal aureole gold (TAG) system, in Muhling et al., eds, SEG 2004 Predictive Mineral Discovery Under Cover Extended Abstracts, 199–203.

Wang, H., Cheng, Q., Zuo, R., 2015. Spatial characteristics of geochemical patterns related to Fe mineralization in the southwestern Fujian province (China). J. Geochem. Explor. 148, 259–269.

Wang, Q., Deng, J., Liu, H., Yang, L., Wan, L., Zhang, R., 2010. Fractal models for ore reserve estimation. Ore Geol. Rev. 37, 2–14.

Wang, Y., Jiao, J.J., 2014. Multivariate statistical analyses on the enrichment of arsenic with different oxidation states in the Quaternary sediments of the Pearl River Delta, China. J. Geochem. Explor. 138, 72–80.

Yang, J., Cheng, Q., 2015. A comparative study of independent component analysis with principal component analysis in geological objects identification, Part I: Simulations. J. Geochem. Explor. 149, 127–135.

Yasrebi, A.B., 2014. Determination of an Ultimate Pit Limit Utilising Fractal Modelling to Optimise NPV. Published PhD Thesis, University of Exeter Publisher, Exeter, UK.

Yousefi, M., Kamkar-Rouhani, A., Carranza, E.J.M., 2012. Geochemical mineralization probability index (GMPI): a new approach to generate enhanced stream sediment geochemical evidential map for increasing probability of success in mineral potential mapping. J. Geochem. Explor. 115, 24–35.

Yousefi, M., Kamkar-Rouhani, A., Carranza, E.J.M., 2014. Application of staged factor analysis and logistic function to create a fuzzy stream sediment geochemical evidence layer for mineral prospectivity mapping. Geochem. Explor. Environ. Anal Online available.

Yousefi, M., Carranza, E.J.M., 2015. Prediction–area (P–A) plot and C-A fractal analysis to classify and evaluate evidential maps for mineral prospectivity modeling. Comput. Geosci. 79, 69–81.

Yousefi, M., 2016. Recognition of an enhanced multi-element geochemical signature of porphyry copper deposits for vectoring into mineralized zones and delimiting exploration targets in Jiroft area, SE Iran. HYPERLINK "http://www.sciencedirect.com/science/journal/01691368" \o "Go to Ore Geology Reviews on ScienceDirect" Ore Geology Reviews, http://dx.doi.org/10.1016/j.oregeorev.2016.12.024.

Zuo, R., 2011. Identifying geochemical anomalies associated with Cu and Pb-Zn skarn mineralization using principal component analysis and spectrum-area fractal modelling in the Gangdese Belt, Tibet (China). J. Geochem. Explor. 111, 13–22.

Zuo, R., 2012. Exploring the effects of cell size in geochemical mapping. J. Geochem. Explor. 112, 357–367.

Zuo, R., 2014. Identification of geochemical anomalies associated with mineralization in the Fanshan district, Fujian, China. J. Geochem. Explor. 139, 170–176.

Zuo, R., Carranza, E.J.M., Cheng, Q., 2012. Fractal/multifractal modelling of geochemical exploration data. J. Geochem. Explor. 122, 1–3.

Zuo, R., Cheng, Q., 2008. Mapping singularities: a technique to identify potential Cu mineral deposits using sediment geochemical data, an example for Tibet, west China. Mineral. Mag. 72, 531–534.

Zuo, R., Cheng, Q., Agterberg, F.P., Xia, Q., 2009. Application of singularity mapping technique to identify local anomalies using stream sediment geochemical data, a case study from Gangdese, Tibet, western China. J. Geochem. Explor. 101, 225–235.

Zuo, R., Wang, J., 2016. Fractal/multifractal modeling of geochemical data: a review. J. Geochem. Explor. 164, 33–41.

Zuo, R., Wang, J., Chen, G., Yang, M., 2015. Identification of weak anomalies: a multifractal perspective. J. Geochem. Explor. 148, 12–24.

Zuo, R., Xia, Q., Wang, H., 2013. Compositional data analysis in the study of integrated geochemical anomalies associated with mineralization. Appl. Geochem. 28, 202–221.